

Diversifying NMR Supersequences with New HSQC-based Modules

Jonathan R. J. Yong,¹ Alexandar L. Hansen,² Ēriks Kupče,³ Tim D. W. Claridge^{1,*}

¹ *Chemistry Research Laboratory, Department of Chemistry, University of Oxford, Mansfield Road, Oxford, OX1 3TA, U.K.*

² *Campus Chemical Instrument Center, The Ohio State University, 460 W. 12th Avenue, Columbus, OH, 43210 U.S.*

³ *Bruker UK Ltd., Banner Lane, Coventry, CV4 9GH, U.K.*

* tim.claridge@chem.ox.ac.uk

Abstract

The sensitivity-enhanced HSQC, as well as HSQC-TOCSY, experiments are incorporated into NOAH (NMR by Ordered Acquisition using ^1H detection) supersequences, adding diversity for ^{13}C and ^{15}N modules. Importantly, these heteronuclear modules are specifically tailored to preserve the magnetisation required for subsequent acquisition of homonuclear modules in a supersequence. In addition, we present protocols for optimally combining HSQC and HSQC-TOCSY elements within the same supersequences, yielding high-quality 2D spectra suitable for structure characterisation but with greatly reduced experiment durations.

In recent years, there has been significant interest in the acceleration of multidimensional NMR data acquisition.^{1–5} In particular, some of the more readily implemented methods involve multiple-FID experiments which use either single or multiple receivers. Of these, one of the most versatile approaches is to utilise different “pools” of magnetisation available within a sample for the sequential collection of different spectra without an intervening recovery delay, as exemplified by the NOAH (NMR by Ordered Acquisition using ^1H detection) technique.⁶ Virtually all of the most common 2D experiments used in small molecule characterisation, such as HSQC, HMBC, COSY, TOCSY, NOESY, and ROESY, can be concatenated in a modular fashion to form *supersequences*

which collectively use only one recovery delay (d_1) (Figure 1a). As the recovery delay accounts for the large majority of experiment time in 2D NMR, the NOAH approach can provide time savings of up to $\sim 4\times$ compared to the conventional individual acquisition of each spectrum, where each constituent experiment would require its own recovery delay.

One-bond heteronuclear correlation experiments, namely HSQC and HMQC, play a central role in the structural elucidation of small organic molecules and biomolecules.⁷ These experiments are also a core component of many NOAH experiments, since the magnetisation they use (protons directly coupled to isotopically dilute X nuclei, i.e. ^{13}C or ^{15}N) can be efficiently differentiated from the “bulk” magnetisation of protons that are not directly attached to these NMR-active nuclei.⁸ Following the notation of Orts,⁹ we refer to these two magnetisation components (proton coupled to X and proton not coupled to X) as $^1\text{H}^X$ and $^1\text{H}^{\text{IX}}$ respectively. At the same time, due to the low natural abundance of these heteronuclei, these spectra are typically less sensitive than the homonuclear spectra that are placed towards the end of the supersequence. Consequently, for dilute samples, the minimum experimental time is generally dictated by these heteronuclear experiments, meaning any improvements in experiment sensitivity can be directly translated into greater time savings.

In the 1990s, Cavanagh, Rance, and Kay introduced the sensitivity-enhanced HSQC (seHSQC) experiment,¹⁰ which improves on the sensitivity of an ordinary echo–antiecho HSQC by up to a factor of 2 in the most ideal case. This is accomplished through the so-called preservation of equivalent pathways (PEP) scheme, which converts two magnetisation components that are cosine- and sine-modulated in t_1 into observable magnetisation prior to detection.¹¹ Here, we show how the original seHSQC sequence can be modified such that it can be used as a NOAH module. We add further diversification by incorporating a HSQC-TOCSY module, derived from the ASAP-HSQC-TOCSY,^{1g} that is also compatible with the NOAH strategy. Both of these modules can be inserted either independently or together into NOAH supersequences, allowing large amounts of chemical information to be acquired in short times.

A typical example of a NOAH supersequence is the NOAH-4 MSCN experiment (Figure 1a), which

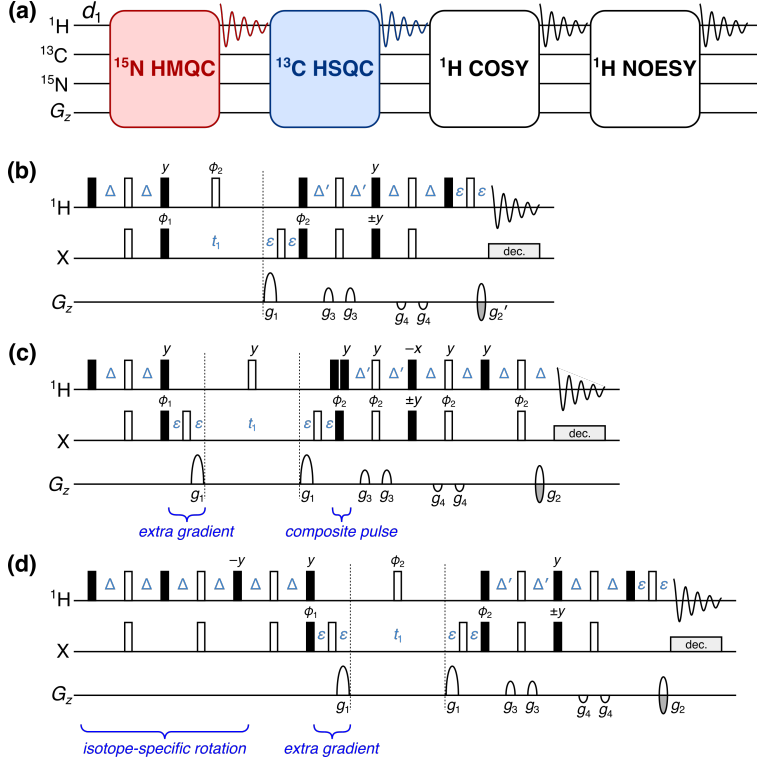


Figure 1: (a) Overview of a typical NOAH supersequence (MSCN, using the single-letter abbreviations previously defined^{6a}). The ¹⁵N–¹H HMQC and ¹³C–¹H HSQC modules are coloured; these may be replaced with the new seHSQC module proposed in this work. (b) Cavanagh–Rance–Kay (CRK) seHSQC.¹⁰ (c) Version 1 of the NOAH seHSQC module, abbreviated as “S₁⁺”. (d) Version 2 of the NOAH seHSQC module, abbreviated as “S₂⁺”. Filled and unfilled bars represent 90° and 180° pulses respectively; all 180° pulses on ¹³C are adiabatic (swept-frequency) pulses. All pulses are applied along +x unless otherwise noted. Phase cycling is performed with $\phi_1 = (x, -x)$ and $\phi_2 = (x, x, -x, -x)$. The delays are chosen as follows: $\Delta = 1/(4 \cdot ^1J_{\text{XH}})$, $\Delta' = 1/(8 \cdot ^1J_{\text{CH}})$ or $1/(4 \cdot ^1J_{\text{NH}})$, and ε is the minimum time needed for a gradient pulse and subsequent recovery. All gradient pulses are 1 ms long, except for g_1 and g_2 in ¹⁵N experiments which are 2.5 ms long. Gradient amplitudes, as percentages of maximum gradient strength, are as follows: $g_1 = 80\%$; $g_2 = \pm 40.2\%$ (¹³C) or $\pm 16.2\%$ (¹⁵N); $g_2' = g_2/2$; $g_3 = 11\%$; $g_4 = -5\%$. The signs of g_2 and g_2' , as well as the phase of the 90° X pulse marked $\pm y$, are alternated within each t_1 increment to provide echo–antiecho selection. Refer to Figure S1 for product operator analysis.

yields ¹⁵N HMQC, ¹³C HSQC, COSY, and NOESY spectra in one single experiment.^{6a} The implementation of this supersequence relies on the fact that the output of any one module contains all the necessary magnetisation components required for downstream modules. For example, both the standard NOAH HMQC (Figure S1a)^{1b,6a} and HSQC (Figure S1b)^{1e,6a} modules return the bulk ¹H^{IX} magnetisation back to its equilibrium position (+z). In the MSCN sequence, this bulk magnetisation can therefore be used as the input to the COSY and NOESY homonuclear modules which follow. However, the original Cavanagh–Rance–Kay (CRK) seHSQC (Figure 1b) does not

obey this principle: it causes bulk magnetisation to be dephased by coherence transfer pathway (CTP) gradients. Consequently, downstream modules can only utilise any bulk $^1\text{H}^{1\text{X}}$ magnetisation that has relaxed during the HSQC FID acquisition, leading to drastic losses in signal intensity. This is illustrated using a NOAH-2 S^+C^c (seHSQC + CLIP-COSY¹²) supersequence: while the CRK seHSQC implementation (Figure 2a) affords significant sensitivity gains (primarily for CH peaks, as predicted by theory¹³), the COSY module which follows suffers from an almost complete ($\sim 90\%$) loss of intensity. While one could argue that this is still tolerable for the COSY module, which is the most sensitive of all NOAH modules, these losses are not permissible for less inherently sensitive homonuclear modules such as NOESY and ROESY.

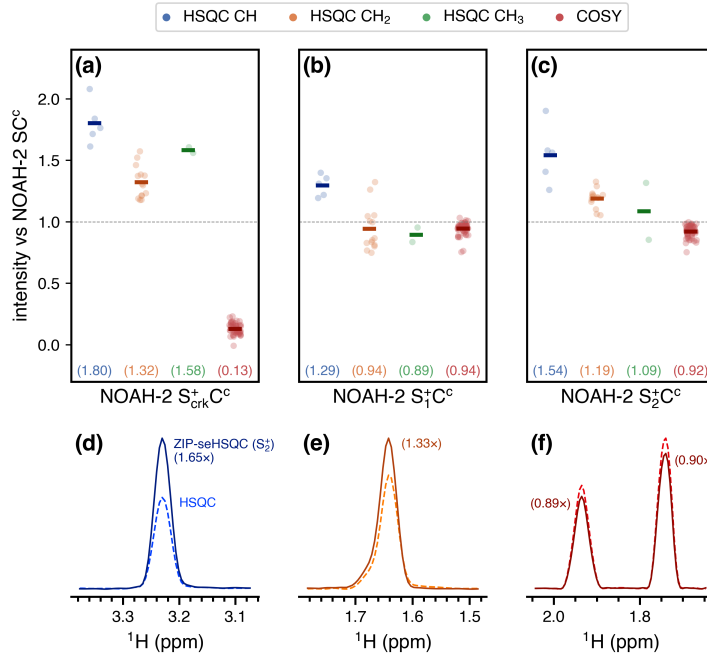


Figure 2: Sensitivity comparisons for NOAH-2 S^+C^c (seHSQC + CLIP-COSY) supersequences, using the CRK and NOAH seHSQC implementations. The delay Δ' was set to $1/(8 \cdot ^1J_{\text{CH}})$. All intensities are normalised against the NOAH-2 SC^c (HSQC + CLIP-COSY) supersequence, without HSQC sensitivity enhancement. HSQC intensities are further grouped by multiplicity. Circles represent the relative intensities of individual peaks; solid bars, as well as the numbers in parentheses, indicate averages over all peaks of a given type. (a) Using the original CRK seHSQC (Figure 1b). The CRK seHSQC does not preserve the bulk $^1\text{H}^{1\text{X}}$ magnetisation, leading to severely reduced COSY intensities. (b) Using the S_1^+ module (Figure 1c). (c) Using the S_2^+ module (Figure 1d). (d)–(e) Slices of the NOAH HSQC (dashed line) and NOAH ZIP-seHSQC (S_2^+) spectra (solid line) through $f_1 = 78.9$ ppm (a CH peak, (d)) and $f_1 = 28.5$ ppm (a CH₂ peak, (e)). (f) Slices of the CLIP-COSY module from the NOAH-2 SC^c (dashed line) and S_2^+C^c (solid line) supersequences, through $f_1 = 1.36$ ppm. Spectra were obtained on a 700 MHz Bruker AV III equipped with a TCI H/C/N cryoprobe; the sample used was 40 mM andrographolide in DMSO-*d*₆.

In this work, we compare two possible solutions to this, which form the basis of the NOAH seHSQC modules. In both cases, we require a pulse sequence element which performs a selective 90° rotation on $^1\text{H}^X$ magnetisation and leaves $^1\text{H}^{!X}$ magnetisation untouched. The first version of the NOAH seHSQC (Figure 1c) uses a composite ^1H pulse immediately following t_1 to accomplish this aim, as both magnetisation components have already diverged by this point. On the other hand, the second (Figure 1d) actively differentiates the two components at the start of the sequence by prepending a double heteronuclear spin echo, a strategy recently reported by Hansen *et al.*¹⁴ This zz isotope-selective (ZIP) pulse element is based on the observation that the bulk $^1\text{H}^{!X}$ magnetisation in the seHSQC will be returned to $+z$ if the phase of the initial ^1H 90_x° pulse in the CRK seHSQC is changed by 90° to $+y$. To generate the required HSQC signal, however, a similar pulse also needs to be applied along $+x$. Overall, what is required is therefore a pulse sequence element which simultaneously acts as a 90_x° (or 90_{-x}°) pulse on protons coupled to spin-X, and as a 90_y° pulse on uncoupled protons. The resulting ZIP element is similar to the zz -filter, which has previously been used in the NOAH zz -HMBC module to retain the magnetisation of directly coupled protons for a subsequent HSQC module.^{6b,6d} However, the ZIP element has different pulse phases to this and consequently leads to a different overall outcome, i.e. 90_{-x}° on $^1\text{H}^X$ and 90_y° on $^1\text{H}^{!X}$.

In addition to the aforementioned modifications, both NOAH seHSQC modules also contain a CTP gradient prior to the t_1 period (highlighted in Figures 1c and 1d). In the S_1^+ module, the $^1\text{H}^{!X}$ magnetisation is in the xy -plane during t_1 (see Figure S1 for product operator analysis), and would simply be dephased if this gradient were not present, making its presence mandatory. Alternatively, the S_2^+ module places the $^1\text{H}^{!X}$ magnetisation on $\pm z$ in t_1 . This gradient is therefore not used for rephasing, but instead serves to suppress artefacts in downstream modules, which would otherwise arise from bulk magnetisation that (due to pulse imperfections) is *not* longitudinal and can therefore evolve during either half of the HSQC t_1 period (Figures S2 to S4). This magnetisation then evolves again in the t_1 period of a later homonuclear module (e.g. COSY), resulting in each COSY peak with indirect-dimension frequency $f_1 = \Omega_H$ being accompanied by a pair of “wing” artefacts at $f_1 = \Omega_H \pm (\Omega_H \cdot \text{SW}_{\text{COSY}})/(2 \cdot \text{SW}_{\text{HSQC}})$, where Ω_H and SW refer to the proton offset and indirect-dimension spectral width respectively (both in Hz). Importantly, the artefacts arising from diagonal

peaks can have intensities that are comparable to genuine crosspeaks (Figure S2), which highlights the importance of suppressing these artefacts. Apart from the “wing” artefacts in downstream modules, we also briefly note here that the presence of two CTP gradients inside the seHSQC t_1 period allows the final CTP gradient (g_2) to have twice its usual amplitude, thereby providing additional artefact suppression in the seHSQC itself. This is particularly important in the $^{15}\text{N}-^1\text{H}$ seHSQC, as will be explained below.

Both NOAH seHSQC modules provide clear sensitivity gains over the NOAH HSQC module for CH peaks (Figures 2b to 2d). For CH_2 and CH_3 peaks, when the delay Δ' is set to $1/(8 \cdot ^1J_{\text{CH}})$ as done here, the gains that can be achieved via sensitivity enhancement are rather more modest (the case where $\Delta' = 1/(4 \cdot ^1J_{\text{CH}})$ is explored in Figure S5).^{13a} Furthermore, the modifications present in the NOAH seHSQC invariably make them less efficient as compared to the original CRK implementation. Consequently, in this example, the use of the S_1^+ module does not provide any sensitivity enhancement for CH_2 and CH_3 peaks, whilst the S_2^+ module yields on average $1.19\times$ increased sensitivity for CH_2 peaks (Figure 2e). The new seHSQC modules, however, bring about dramatic improvements in the homonuclear module which follows. In contrast to the CRK seHSQC, which largely destroys the requisite bulk magnetisation, both seHSQC modules preserve the majority of it, performing >90% as well as the original HSQC module (Figure 2f). We note that the BIG-BIRD element reported by Briand and Sørensen,^{8d} which independently excites $^1\text{H}^X$ and $^{1\text{H}}\text{H}^X$ magnetisation with arbitrary flip angles and phases, is also capable of performing the same role as the ZIP element in the S_2^+ module. However, we find that the ZIP provides greater signal-to-noise in both the seHSQC itself as well as downstream modules (Figure S6).

Multiplicity editing¹⁵ can be easily incorporated into both NOAH seHSQC sequences (Figure S7) by expanding the spin echo immediately following t_1 . As described previously, the S_1^+ module places the bulk magnetisation in the xy -plane during the editing period; the same is true of the unenhanced NOAH HSQC. In these modules, the bulk $^1\text{H}^X$ magnetisation is therefore subject to homonuclear coupling (J_{HH}) evolution, leading to a small decrease in the sensitivity of later homonuclear modules when multiplicity editing is introduced. Since homonuclear experiments typically have a greater inherent sensitivity than the (se)HSQC, this minor loss is rarely a problem, and is far outweighed

by the benefits of incorporating multiplicity editing in the HSQC. Nevertheless, the fact that the S_2^+ module does not suffer from such a penalty is a welcome benefit. As a result, when editing is included, the S_2^+ module slightly outperforms both the S and S_1^+ modules by around 10% in terms of preserving bulk magnetisation (Figure S8).

The proposed seHSQC module can be similarly implemented for ^{15}N experiments. Currently, in NOAH supersequences, $^{15}\text{N}-^1\text{H}$ correlations are primarily obtained using the HMQC module;^{1b,6a} compared to this, the new S_2^+ module can provide greater than $4\times$ enhanced sensitivity (Figure 3). This arises partly because the PEP sensitivity enhancement scheme can be optimised for NH peaks by setting the reverse INEPT transfer delay Δ' to be equal to $1/(4 \cdot ^1J_{\text{NH}})$. However, there is also a significant improvement due to the fact that peaks in the ^{15}N seHSQC are not broadened in the indirect dimension by J_{HH} , unlike in the ^{15}N HMQC. Although the S_2^+ module retains a slightly smaller amount of $^1\text{H}^{15}\text{N}$ magnetisation ($\sim 70\%$, versus $\sim 80\%$ for the HMQC (Figure S9)), this is unlikely to be problematic, since it is the ^{15}N module which typically has the lowest intrinsic sensitivity in a supersequence.

Although the S and S_1^+ modules also provide sensitivity gains versus the HMQC, they both come with other drawbacks. As previously discussed, these two modules place bulk $^1\text{H}^{15}\text{N}$ magnetisation in the xy -plane during the t_1 period. Consequently, the amount of bulk magnetisation that is retained decreases as t_1 is lengthened, leading to line broadening in the indirect dimensions of all downstream modules (Figure S10). Whilst this is not a problem with the ^{13}C HSQC where typical ^{13}C indirect dimension acquisition times are relatively short, the smaller spectral widths in ^{15}N experiments can mean downstream modules suffer moderate losses in both sensitivity and resolution. The S_2^+ module avoids this issue entirely, making it especially well-suited to obtaining ^{15}N correlations; we henceforth refer to it as the S_N^+ module.

One remaining potential issue in the S_N^+ module arises from the cumulative effects of pulse imperfections, which cause a portion of bulk $^1\text{H}^{15}\text{N}$ magnetisation to be transverse just prior to detection of the seHSQC signal. Although this only represents a small fraction of the bulk magnetisation, if left uncontrolled, the resulting artefacts typically have intensities that are comparable to the

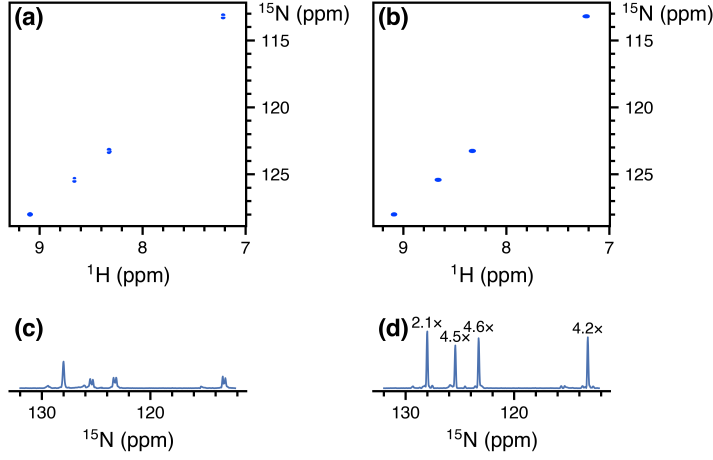


Figure 3: Comparison of the ^{15}N - ^1H seHSQC module (S_2^+) with the standard NOAH HMQC module (M), taken from NOAH-3 XS $^+ \text{C}^c$ supersequences (^{15}N experiment + ^{13}C seHSQC + CLIP-COSY). The S_1^+ module is not shown here as it causes line broadening downstream modules (see text). (a) ^{15}N HMQC spectrum. (b) ^{15}N seHSQC spectrum. (c) Projection of HMQC onto the f_1 axis. Splitting due to J_{HH} is clearly visible for three of the four peaks. (d) Projection of seHSQC onto the f_1 axis. Signal-to-noise improvements relative to the HMQC spectrum are indicated over each peak. The largest gains are observed for peaks where the multiplet structure is collapsed; however, even in the absence of that, a $\sim 2\times$ gain is still obtained. Spectra were obtained on a 700 MHz Bruker AV III equipped with a TCI H/C/N cryoprobe; the sample used was 40 mM gramicidin in DMSO- d_6 .

seHSQC crosspeaks (Figure S11). The key to suppressing these artefacts efficiently lies in the final CTP gradient g_2 (Figure 1d), which dephases any transverse bulk magnetisation. The S_N^+ module therefore greatly benefits from having two CTP gradients g_1 within the t_1 period, as this means that g_2 will have twice its usual amplitude. For optimal performance, however, one further modification proves beneficial: the CTP gradients g_1 and g_2 should all be lengthened from their typical duration of 1 ms, in order to provide more effective dephasing. In practice, we find that gradient durations of 2 to 2.5 ms provide excellent artefact suppression whilst not causing any appreciable difference in the intensity of the desired crosspeaks (Figure S11). These extended gradients are not required in the ^{13}C seHSQC for two reasons: firstly, the amplitude of g_2 in the ^{13}C seHSQC is larger by a factor of $\gamma_{\text{C}}/\gamma_{\text{N}} \approx 2.5$; and secondly, the greater natural abundance of ^{13}C (1.1% versus 0.36% of ^{15}N) leads to an intrinsically larger signal intensity, which makes any residual artefacts less apparent.

In scenarios where high resolution in the ^{15}N dimension is not required, it can prove useful to reduce

the number of t_1 increments and in its place increase the number of transients acquired.^{3d,3e} In new versions of the NOAH pulse programmes (including those provided in the *Supporting Information*), this feature can be enabled by specifying a factor k by which to perform this scaling. Note that the scaling is only applied to the ^{15}N module; all other modules are left untouched. In our hands, setting $k = 2$ or 4 for the original ^{15}N HMQC can lead to significant sensitivity gains of up to $\sim 2\times$, since J_{HH} splitting in the indirect dimension tends not to be resolved (Figure S12). This point is not relevant to the seHSQC, and here k -scaling employed in isolation has only a tiny effect on peak height (and signal-to-noise), since any sensitivity gained from the extra transients is typically offset by the broadening (Figure S13). However, the later t_1 increments which were not acquired can be reconstructed using linear projection¹⁶ to mitigate this line broadening. The resulting spectra display sensitivity gains of up to a factor of k , although the fidelity of the reconstruction can suffer for large k , particularly with the HMQC (Figures S14 and S15).

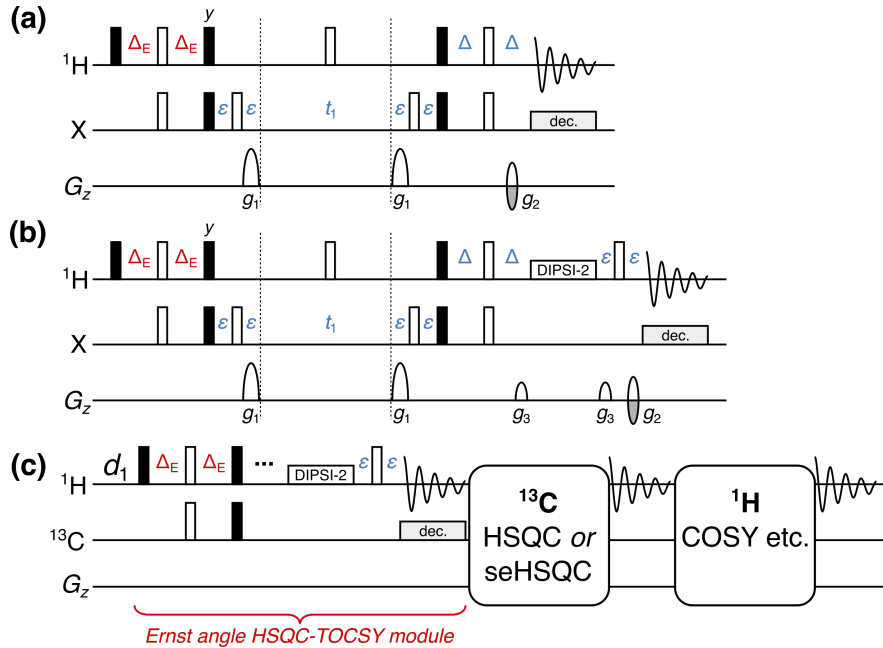


Figure 4: (a) NOAH HSQC module with modified INEPT delay $\Delta_E = (\sin^{-1} f)/(4 \cdot ^1J_{\text{CH}})$, where f is the fraction of ^{13}C magnetisation excited. (b) NOAH HSQC-TOCSY module (“S^T”), modified from the ASAP-HSQC-TOCSY.^{1g} The gradients g_3 are 1 ms long, and are set to 19% of the maximum gradient amplitude. (c) Overview of a NOAH-3 S^TSX or S^TS⁺X supersequence. The ^{13}C magnetisation is partly used by the initial HSQC-TOCSY module, with a subsequent HSQC or seHSQC using the remaining ^1H magnetisation. The bulk ^1H magnetisation is retained for one or more homonuclear modules at the end. All other symbols have the same meanings as in Figure 1.

Next, we note that the HSQC module (though not the new seHSQC modules) allows an arbitrary amount of $^1\text{H}^{\text{C}}$ magnetisation to be excited, with the remainder returned to $+z$.^{1d,1e,1f} In order to excite a proportion f of $^1\text{H}^{\text{C}}$ magnetisation ($0 < f \leq 1$), the initial INEPT delay must be shortened by a factor of $\sin^{-1} f$ (Figure 4a). The remaining $(1 - f)$ of the magnetisation, plus any that relaxes during the HSQC FID, can then be used for a *second* HSQC-based module in the same supersequence. Such a scheme proves to be useful for simultaneously collecting ^{13}C -decoupled and coupled HSQC spectra, or HSQC spectra with different spectral widths. This has previously been accomplished in a multi-FID acquisition (MFA) scheme by keeping the two CTPs in the CRK seHSQC separate, with the cosine- and sine-modulated CTPs each contributing to one spectrum.¹⁷ With the present NOAH strategy, for values of f that are close to 1, the amount of $^1\text{H}^{\text{C}}$ magnetisation regained through relaxation can reach almost 50%. Consequently, by setting $f \approx 0.8$, we can obtain two HSQC spectra with sensitivities that are comparable to the existing MFA approach. Furthermore, the sensitivity of the second HSQC can be boosted by using the new seHSQC modules in its place, in particular the S_2^+ module (Figure S16).

By adding a period of isotropic mixing prior to detection, the NOAH HSQC module may be converted to a HSQC-TOCSY module (denoted by “ S^T ”, Figure 4b). This is similar to the previously reported ASAP-HSQC-TOCSY,^{1g} the key difference being that in the present NOAH context, unused $^1\text{H}^{\text{C}}$ as well as bulk $^1\text{H}^{1\text{C}}$ magnetisation is preserved for use in other modules, instead of later t_1 increments as in the ASAP experiment. Compared to the existing MFA HSQC-TOCSY/HSQC experiment,^{17a} our approach has several characteristics which make it particularly amenable to use in NOAH supersequences. Firstly, the vast majority of $^1\text{H}^{1\text{C}}$ magnetisation is preserved, as required for homonuclear module(s) to be appended in a NOAH supersequence (Figure 4c); in practice, we observe small $^1\text{H}^{1\text{C}}$ losses of ca. 10% due to sequence imperfections. In contrast, the MFA sequence, much like the original CRK seHSQC on which it is based, dephases $^1\text{H}^{1\text{C}}$ magnetisation and causes a 80–90% sensitivity loss in downstream spectra. Secondly, since each NOAH module is independently executed, the NOAH approach allows multiplicity editing to be enabled for only the HSQC and not the HSQC-TOCSY, where accidental overlap may lead to crosspeaks being lost unexpectedly. Lastly, the sensitivity of both spectra in a NOAH experiment can be opti-

mised through the value of f ; this allows a larger amount of $^1\text{H}^{\text{C}}$ magnetisation to be used for the inherently less sensitive HSQC-TOCSY. In our experience, setting $f = 0.9$ provides a good balance for S^TS combinations: the sensitivity in the HSQC is boosted not only by relaxation during the HSQC-TOCSY FID, but also by the isotropic mixing in the HSQC-TOCSY module, which effects a degree of $^1\text{H}^{\text{C}} \rightarrow ^1\text{H}^{\text{C}}$ polarisation transfer (Figure S17). Alternatively, the signal intensity of the HSQC-TOCSY can be maximised by replacing it with the seHSQC-TOCSY module, derived from the S₂⁺ module.¹⁴ The sole drawback of the seHSQC-TOCSY is that it does not allow for variable $^1\text{H}^{\text{C}}$ excitation and therefore cannot preserve any magnetisation for HSQC modules that follow it (Figure S18).

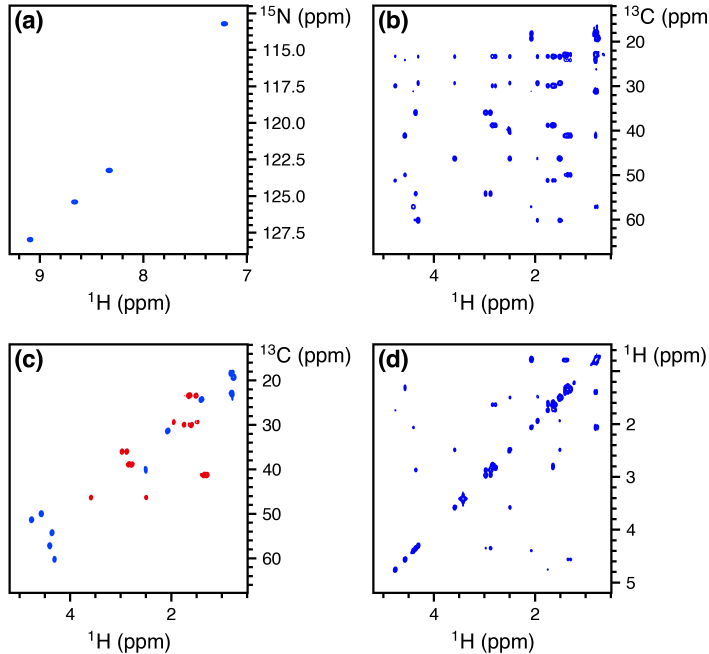


Figure 5: Spectra obtained from the NOAH-4 S_N⁺S^TS₂⁺C^c supersequence. 256 t_1 increments were used, with 2 scans per increment. The total experiment time was 17 minutes and 35 seconds. (a) ^{15}N seHSQC. (b) ^{13}C HSQC-TOCSY (30 ms mixing, $f = 0.9$). (c) Multiplicity-edited ^{13}C ZIP-seHSQC. Notice that having the edited seHSQC removes the need for the less desirable HSQC-TOCSY editing. (d) CLIP-COSY. Spectra were obtained on a 700 MHz Bruker AV III equipped with a TCI H/C/N cryoprobe; the sample used was 40 mM gramicidin (a cyclic decapeptide; (Val–Orn–Leu–D-Phe–Pro)₂) in DMSO-*d*₆.

There exist many ways in which the new modules discussed above can be included in practical experiments for structure characterisation. Here, we illustrate this with the NOAH-4 S_N⁺S^TS₂⁺C^c (^{15}N seHSQC, ^{13}C HSQC-TOCSY, ^{13}C seHSQC, and CLIP-COSY) supersequence (Figure 5). While

individual collection of the four spectra above required 57 minutes and 8 seconds, the NOAH-4 supersequence took only 17 minutes and 35 seconds; this is 30.8% of the original duration, or equivalently a $3.25\times$ speedup. For typical organic molecules, new supersequences such as the NOAH-4 $S^T S_2^+ CT$ allow the rapid and complete collection of C–H and H–H correlations (Figure S19). Experiment times can be further reduced through the use of non-uniform sampling¹⁸ (Figure S20), which is compatible with nearly all of the supersequences shown here (the only exceptions being when k -scaling is employed in ¹⁵N modules, or when COSY modules are recorded without phase-sensitive detection). One can also prepend the NOAH *zz*-HMBC module (“B”);^{6d} this uses the semi-adiabatic *zz*-filter to preserve both ¹H^C and ¹H^N magnetisation, which can then be sampled in the HSQC-based modules presented here (Figure S21).

The new seHSQC and HSQC-TOCSY implementations add to the preexisting variety of NOAH modules, expanding the number of plausible NOAH supersequences tailored for small molecule characterisation. The controlled manipulation of all proton magnetisation reservoirs present within a sample is required for the success of these modules within nested experiments. We have demonstrated the optimisation of the individual HSQC-based modules and their combinations to further enhance the diversity of NOAH supersequences for efficient data collection.

Experimental

All spectra were recorded on a Bruker AV III NMR spectrometer operating at 700 MHz ¹H frequency equipped with a TCI H/C/N cryoprobe. Unless otherwise specified, spectra were recorded with 16 dummy scans, 2 scans per t_1 increment, 256 t_1 increments per module, and a 1.5 s recovery delay. 1024 points were recorded in each FID, leading to an acquisition time of 60.8–73.1 ms depending on the ¹H spectral width (10–12 ppm). The delays in the HSQC sequences were optimised for $^1J_{CH} = 145$ Hz and $^1J_{NH} = 90$ Hz respectively, and the CLIP-COSY mixing delay (denoted by Δ in the original work¹²) was set to 16.7 ms (corresponding to a nominal J_{HH} value of 30 Hz). DIPSI-2 mixing in the HSQC-TOCSY was applied with a B_1 amplitude of 10 kHz.

All NOAH data were processed using the `splitx_au` AU programme, which separates the individual modules into different datasets; these were then individually processed with `noah_EXPT` AU

programmes, which define other processing parameters such as window functions. All datasets were linear predicted up to 512 complex points in f_1 , then zero-filled to 1024 and 2048 complex points in f_1 and f_2 respectively. NUS experiments, such as that in Figure S20, can be set up using a new `noah_nus2.py` Python script. The pulse sequences used here, all AU processing scripts, as well as the NUS Python script are available from the authors upon request, and will also be made available via the online Bruker User Library.

Acknowledgements

J.R.J.Y. thanks the Clarendon Fund (University of Oxford) and the EPSRC Centre for Doctoral Training in Synthesis for Biology and Medicine (EP/L015838/1) for a studentship, generously supported by AstraZeneca, Diamond Light Source, Defence Science and Technology Laboratory, Evotec, GlaxoSmithKline, Janssen, Novartis, Pfizer, Syngenta, Takeda, UCB, and Vertex. [Helpful discussions...](#) [Other acknowledgements...](#)

References

1. (a) Schanda, P.; Kupče, Ě.; Brutscher, B. *J. Biomol. NMR* **2005**, *33*, 199–211; (b) Kupče, Ě.; Freeman, R. *Magn. Reson. Chem.* **2007**, *45*, 2–4; (c) Furrer, J. *Chem. Commun.* **2010**, *46*, 3396; (d) Schulze-Sünninghausen, D.; Becker, J.; Luy, B. *J. Am. Chem. Soc.* **2014**, *136*, 1242–1245; (e) Schulze-Sünninghausen, D.; Becker, J.; Koos, M. R. M.; Luy, B. *J. Magn. Reson.* **2017**, *281*, 151–161; (f) Koos, M. R. M.; Luy, B. *J. Magn. Reson.* **2019**, *300*, 61–75; (g) Becker, J.; Koos, M. R. M.; Schulze-Sünninghausen, D.; Luy, B. *J. Magn. Reson.* **2019**, *300*, 76–83.
2. (a) Frydman, L.; Scherf, T.; Lupulescu, A. *Proc. Natl. Acad. Sci. U. S. A.* **2002**, *99*, 15858–15862; (b) Frydman, L.; Lupulescu, A.; Scherf, T. *J. Am. Chem. Soc.* **2003**, *125*, 9204–9217; (c) Gal, M.; Mishkovsky, M.; Frydman, L. *J. Am. Chem. Soc.* **2006**, *128*, 951–956; (d) Giraudeau, P.; Shrot, Y.; Frydman, L. *J. Am. Chem. Soc.* **2009**, *131*, 13902–13903; (e) Herrera, A.; Fernández-Valle, E.; Martínez-Álvarez, R.; Molero, D.; Pardo, Z. D.; Sáez, E.; Gal, M. *Angew. Chem. Int. Ed.* **2009**, *48*, 6274–6277; (f) Pardo, Z. D.; Olsen, G. L.; Fernández-Valle,

- M. E.; Frydman, L.; Martínez-Álvarez, R.; Herrera, A. *J. Am. Chem. Soc.* **2012**, *134*, 2706–2715; (g) Donovan, K. J.; Kupče, E.; Frydman, L. *Angew. Chem. Int. Ed.* **2013**, *52*, 4152–4155; (h) Dumez, J.-N. *Prog. Nucl. Magn. Reson. Spectrosc.* **2018**, *109*, 101–134.
3. (a) Sattler, M.; Maurer, M.; Schleucher, J.; Griesinger, C. *J. Biomol. NMR* **1995**, *5*, 97–102; (b) Nolis, P.; Pérez, M.; Parella, T. *Magn. Reson. Chem.* **2006**, *44*, 1031–1036; (c) Nolis, P.; Pérez-Trujillo, M.; Parella, T. *Angew. Chem. Int. Ed.* **2007**, *46*, 7495–7497; (d) Pérez-Trujillo, M.; Nolis, P.; Bermel, W.; Parella, T. *Magn. Reson. Chem.* **2007**, *45*, 325–329; (e) Parella, T.; Nolis, P. *Concepts Magn. Reson.* **2010**, *36A*, 1–23; (f) Nolis, P.; Motiram-Corral, K.; Pérez-Trujillo, M.; Parella, T. *J. Magn. Reson.* **2019**, *298*, 23–30.
4. (a) Kupče, Ē.; Freeman, R.; John, B. K. *J. Am. Chem. Soc.* **2006**, *128*, 9606–9607; (b) Kupče, Ē.; Freeman, R. *J. Am. Chem. Soc.* **2008**, *130*, 10788–10792; (c) Kupče, Ē.; Freeman, R. *J. Magn. Reson.* **2010**, *206*, 147–153; (d) Kupče, Ē.; Freeman, R. *Magn. Reson. Chem.* **2010**, *48*, 333–336; (e) Pudakalakatti, S. M.; Dubey, A.; Jaipuria, G.; Shubhashree, U.; Adiga, S. K.; Moskau, D.; Atreya, H. S. *J. Biomol. NMR* **2014**, *58*, 165–173; (f) Pudakalakatti, S. M.; Dubey, A.; Atreya, H. S. *J. Chem. Sci.* **2015**, *127*, 1091–1097; (g) Kovacs, H.; Kupče, Ē. *Magn. Reson. Chem.* **2016**, *54*, 544–560.
5. (a) Motiram-Corral, K.; Pérez-Trujillo, M.; Nolis, P.; Parella, T. *Chem. Commun.* **2018**, *54*, 13507–13510; (b) Kakita, V. M. R.; Rachineni, K.; Bopardikar, M.; Hosur, R. V. *J. Magn. Reson.* **2018**, *297*, 108–112; (c) Nagy, T. M.; Gyöngyösi, T.; Kövér, K. E.; Sørensen, O. W. *Chem. Commun.* **2019**, *55*, 12208–12211; (d) Nolis, P.; Motiram-Corral, K.; Pérez-Trujillo, M.; Parella, T. *ChemPhysChem* **2019**, *20*, 356–360; (e) Nolis, P.; Motiram-Corral, K.; Pérez-Trujillo, M.; Parella, T. *J. Magn. Reson.* **2019**, *298*, 23–30; (f) Nolis, P.; Parella, T. *Magn. Reson. Chem.* **2019**, *57*, S85–S94; (g) Kakita, V. M. R.; Hosur, R. V. *RSC Adv.* **2020**, *10*, 21174–21179; (h) Nagy, T. M.; Kövér, K. E.; Sørensen, O. W. *J. Magn. Reson.* **2020**, *316*, 106767.
6. (a) Kupče, Ē.; Claridge, T. D. W. *Angew. Chem. Int. Ed.* **2017**, *56*, 11779–11783; (b) Kupče, Ē.; Claridge, T. D. W. *Chem. Commun.* **2018**, *54*, 7139–7142; (c) Claridge, T. D. W.; Mayzel,

- M.; Kupče, Ē. *Magn. Reson. Chem.* **2019**, *57*, 946–952; (d) Kupče, Ē.; Claridge, T. D. W. *J. Magn. Reson.* **2019**, *307*, 106568.
- 7. (a) Claridge, T. D. W., *High-Resolution NMR Techniques in Organic Chemistry*, 3rd ed.; Elsevier: Amsterdam, 2016; (b) Cavanagh, J., *Protein NMR Spectroscopy: Principles and Practice*, 2nd ed.; Academic Press: Burlington, Mass., 2007.
 - 8. (a) Garbow, J. R.; Weitekamp, D. P.; Pines, A. *Chem. Phys. Lett.* **1982**, *93*, 504–509; (b) Wimperis, S.; Freeman, R. *J. Magn. Reson.* **1984**, *58*, 348–353; (c) Uhrin, D.; Liptaj, T.; Kover, K. E. *J. Magn. Reson., Ser. A* **1993**, *101*, 41–46; (d) Briand, J.; Sørensen, O. W. *J. Magn. Reson.* **1997**, *125*, 202–206; (e) Briand, J.; Sørensen, O. W. *J. Magn. Reson.* **1998**, *135*, 44–49.
 - 9. Orts, J.; Gossert, A. D. *Methods* **2018**, *138–139*, 3–25.
 - 10. (a) Palmer, A. G.; Cavanagh, J.; Wright, P. E.; Rance, M. *J. Magn. Reson.* **1991**, *93*, 151–170; (b) Kay, L.; Keifer, P.; Saarinen, T. *J. Am. Chem. Soc.* **1992**, *114*, 10663–10665.
 - 11. (a) Cavanagh, J.; Rance, M. *J. Magn. Reson.* **1990**, *88*, 72–85; (b) Cavanagh, J.; Rance, M. *Annu. Rep. NMR Spectrosc.* **1993**, *27*, 1–58.
 - 12. Koos, M. R. M.; Kummerlöwe, G.; Kaltschnee, L.; Thiele, C. M.; Luy, B. *Angew. Chem. Int. Ed.* **2016**, *55*, 7655–7659.
 - 13. (a) Schleucher, J.; Schwendinger, M.; Sattler, M.; Schmidt, P.; Schedletzky, O.; Glaser, S. J.; Sørensen, O. W.; Griesinger, C. *J. Biomol. NMR* **1994**, *4*, 301–306; (b) Kontaxis, G.; Stonehouse, J.; Laue, E. D.; Keeler, J. *J. Magn. Reson.* **1994**, *111*, 70–76.
 - 14. Hansen, A. L.; Kupče, Ē.; Li, D.-W.; Bruschweiler-Li, L.; Wang, C.; Brüschweiler, R. 2D NMR-based Metabolomics with HSQC/TOCSY NOAH Supersequences, submitted for publication, 2021.
 - 15. Parella, T.; Sánchez-Ferrando, F.; Virgili, A. *J. Magn. Reson.* **1997**, *126*, 274–277.
 - 16. (a) Tufts, D.; Kumaresan, R. *IEEE Trans. Acoust., Speech, Signal Process.* **1982**, *30*, 671–675; (b) Koehl, P. *Prog. Nucl. Magn. Reson. Spectrosc.* **1999**, *34*, 257–299.
 - 17. (a) Nolis, P.; Motiram-Corral, K.; Pérez-Trujillo, M.; Parella, T. *ChemPhysChem* **2019**, *20*, 356–360; (b) Nolis, P.; Motiram-Corral, K.; Pérez-Trujillo, M.; Parella, T. *J. Magn. Reson.* **2019**, *298*, 23–30.

18. (a) Kazimierczuk, K.; Stanek, J.; Zawadzka-Kazimierczuk, A.; Koźmiński, W. *Prog. Nucl. Magn. Reson. Spectrosc.* **2010**, *57*, 420–434; (b) Mobli, M.; Hoch, J. C. *Prog. Nucl. Magn. Reson. Spectrosc.* **2014**, *83*, 21–41; (c) Kazimierczuk, K.; Orekhov, V. *Magn. Reson. Chem.* **2015**, *53*, 921–926; (d) Gołowicz, D.; Kasprzak, P.; Orekhov, V.; Kazimierczuk, K. *Prog. Nucl. Magn. Reson. Spectrosc.* **2020**, *116*, 40–55.

Supporting Information
for
Diversifying NMR Supersequences with New
HSQC-based Modules

Jonathan R. J. Yong,¹ Alexandar L. Hansen,² Ēriks Kupče,³ Tim D. W.
Claridge^{1,*}

¹ *Chemistry Research Laboratory, Department of Chemistry, University of Oxford,
Mansfield Road, Oxford, OX1 3TA, U.K.*

² *Campus Chemical Instrument Center, The Ohio State University, 460 W. 12th Avenue,
Columbus, OH, 43210 U.S.*

³ *Bruker UK Ltd., Banner Lane, Coventry, CV4 9GH, U.K.*

* tim.claridge@chem.ox.ac.uk

Contents

| | |
|-------------------------------------------------------------------------------------------|------------|
| 1 Product operator analysis for pulse sequences | S3 |
| 2 Origin and suppression of wing artefacts | S4 |
| 3 Effect of setting $\Delta' = 1/(4 \cdot {}^1J_{\text{CH}})$ in seHSQC | S8 |
| 4 Comparison of BIG-BIRD and ZIP elements | S9 |
| 5 Multiplicity editing in seHSQC | S10 |
| 6 Summary of ${}^{13}\text{C}$ seHSQC sensitivity comparisons | S11 |
| 7 Retention of bulk magnetisation by ${}^{15}\text{N}$ modules | S13 |
| 8 ${}^{15}\text{N}$ HSQC and line broadening | S14 |
| 9 Effect of lengthened gradients in ${}^{15}\text{N}$ modules | S15 |
| 10 Effect of k-scaling | S16 |
| 11 HSQC-TOCSY/HSQC sensitivity comparisons | S21 |
| 12 Other example spectra | S25 |

1 Product operator analysis for pulse sequences

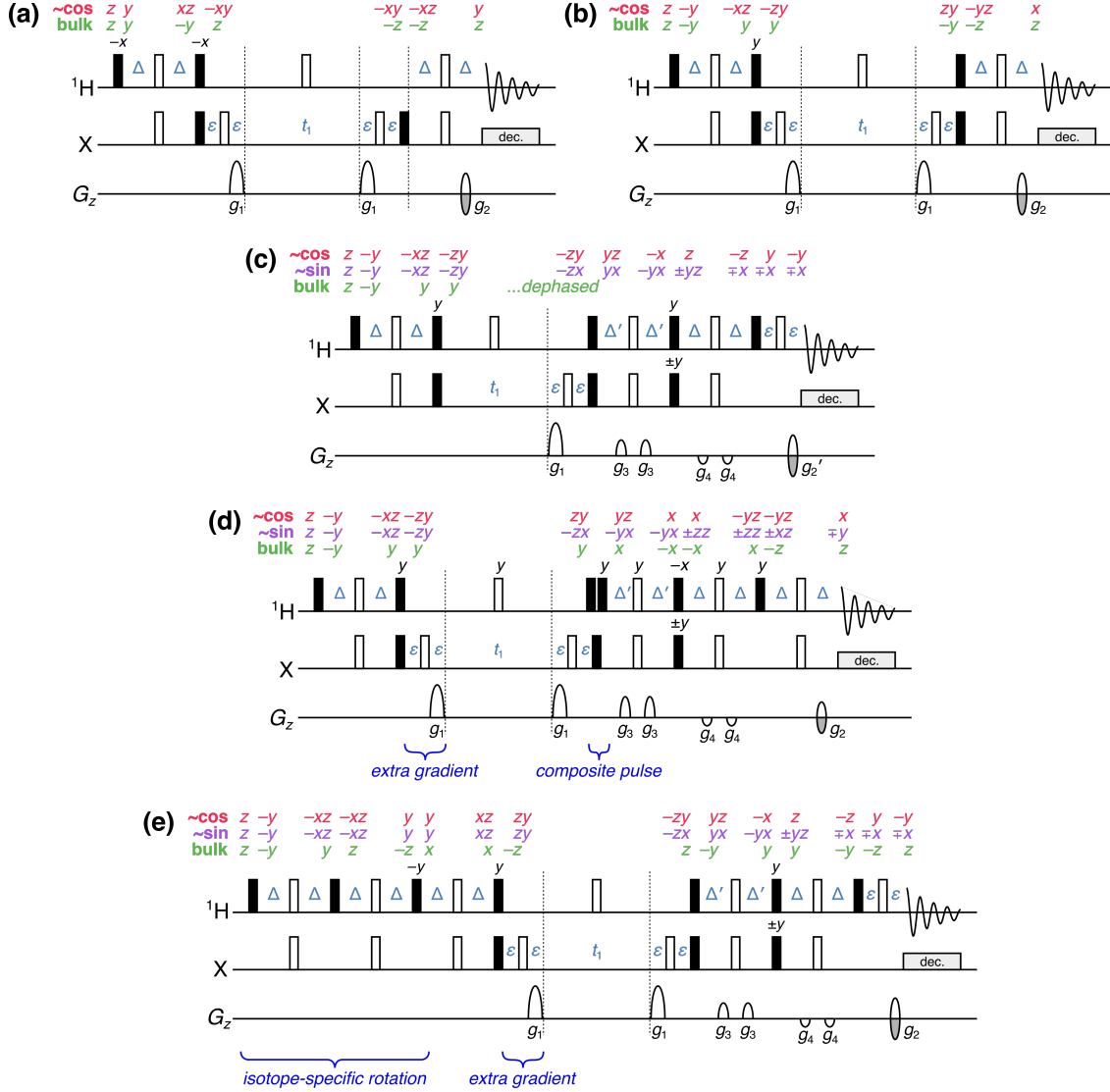


Figure S1: Product operators for an IS spin system at each stage of the HSQC and seHSQC sequences described in the main text. One-letter terms m ($m \in \{x, y, z\}$) are shorthand for single-spin terms on proton, i.e. \hat{I}_m . Two-letter terms mn are shorthand for two-spin terms on both the proton and heteronucleus, i.e. $2\hat{I}_m\hat{S}_n$. “ $\sim\cos$ ” represents the pathway for ${}^1\text{H}^{\text{C}}$ magnetisation that is cosine-modulated after t_1 : for the HMQC and HSQC, this is the only component that is detected. For the seHSQC, the sine-modulated ${}^1\text{H}^{\text{C}}$ component (labelled with “ $\sim\sin$ ”) is also detected. “bulk” refers to the bulk ${}^1\text{H}^{\text{C}}$ magnetisation, i.e. protons that are not directly coupled to the heteronucleus. Note that this analysis assumes $\Delta = \Delta' = 1/(4 \cdot {}^1J_{\text{XH}})$. All other symbols have the same meaning as in Figure 1 of the main text. (a) NOAH HMQC (“M”). (b) NOAH HSQC (“S”). (c) Cavanagh–Rance–Kay seHSQC; notice that the bulk magnetisation is dephased by the lone t_1 gradient. (d) NOAH seHSQC, version 1 (“ S_1^+ ”). (e) NOAH seHSQC, version 2 (“ S_2^+ ”). Immediately following the ZIP pulse sequence element, directly bonded protons are rotated onto $+y$, whereas the bulk magnetisation is rotated onto $+x$.

2 Origin and suppression of wing artefacts

The origin of the “wing” artefacts in the final homonuclear modules can be most clearly seen from the following series of experiments involving the NOAH-3 ^{15}N seHSQC/ ^{13}C ZIP-seHSQC/CLIP-COSY ($\text{S}_\text{N}^+\text{S}_2^+\text{C}^\text{c}$) supersequence. As described in the main text, if the extra gradient before t_1 is not present, each peak in the COSY with an indirect-dimension frequency of $f_1 = \Omega_\text{H}$ is flanked by a pair of artefacts at

$$f_1 = \Omega_\text{H} \pm \Omega_\text{H} \cdot \left(\frac{\text{SW}_{\text{COSY}}}{2 \cdot \text{SW}_{\text{HSQC}}} \right),$$

where Ω_H is the offset of the relevant proton and SW refers to the indirect-dimension spectral width. Since the f_1 spectral widths of the two seHSQC modules are different, they lead to distinct sets of wing artefacts in the COSY. In the spectra shown in the following figures, we have

$$\begin{aligned} \text{SW}_{^{15}\text{N HSQC}} &= 2128 \text{ Hz} \\ \text{SW}_{^{13}\text{C HSQC}} &= 23810 \text{ Hz} \\ \text{SW}_{\text{COSY}} &= 8418 \text{ Hz} \end{aligned}$$

meaning that the artefacts coming from the ^{15}N seHSQC occur at $f_1 = (1.00 \pm 1.98)\Omega_\text{H}$ (and are therefore often folded), whereas artefacts coming from the ^{13}C seHSQC occur at $f_1 = (1.00 \pm 0.18)\Omega_\text{H}$ (and are typically found very close to the main peak). In both cases, the artefacts associated with intense methyl group peaks are the most obvious, but similar artefacts are observed for all other peaks, albeit with lower absolute intensities.

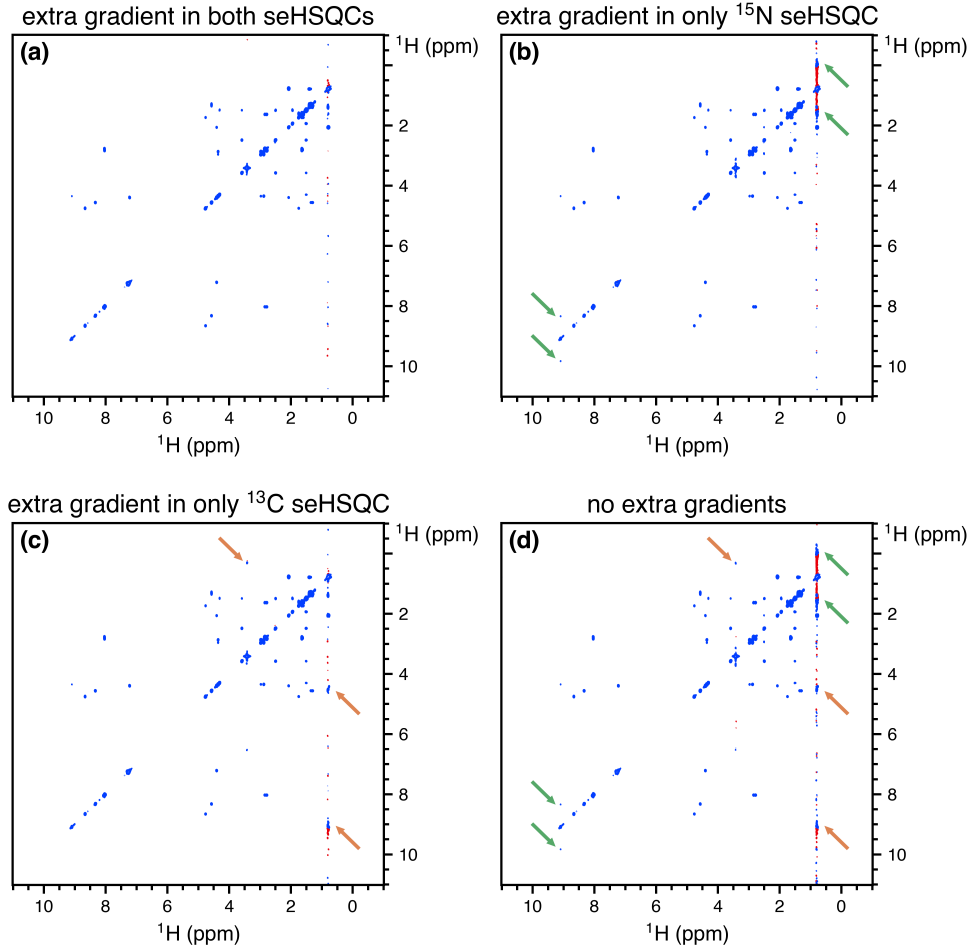


Figure S2: CLIP-COSY spectra obtained from various forms of the NOAH-3 $S_N^+S_2^+C^c$ supersequence. Wing artefacts arising from the ^{15}N seHSQC are highlighted in orange; those arising from the ^{13}C seHSQC in green. Notice how (in this case) the former can easily be misinterpreted as a crosspeak, while the latter obscures genuine crosspeaks. **(a)** With the extra gradient inserted for both modules, i.e. no artefacts. **(b)** With an extra gradient in only the ^{15}N module, i.e. only the ^{13}C artefacts. **(c)** With an extra gradient in only the ^{13}C module. **(d)** With no extra gradients. Spectra were obtained on a 700 MHz Bruker AV III equipped with a TCI H/C/N cryoprobe; the sample used was 40 mM gramicidin in DMSO- d_6 .

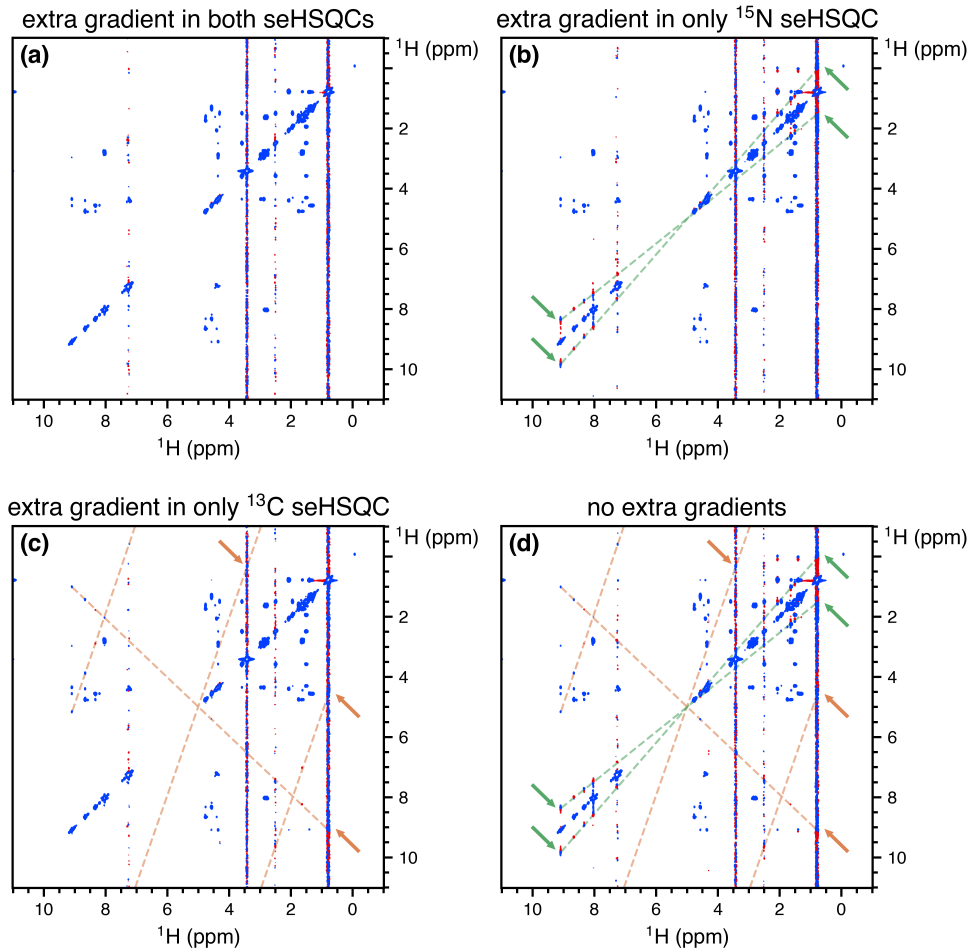


Figure S3: The same spectra as Figure S2, but plotted with a smaller base contour level to illustrate the regular indirect-dimension frequencies of the wing artefacts. A greater number of artefacts are now visible (in addition to those already highlighted in Figure S2, which are still marked with arrows). The artefacts arising from the ^{15}N seHSQC lie on the orange dotted line; those arising from the ^{13}C seHSQC lie on the green dotted line. **(a)** With the extra gradient inserted for both modules, i.e. no artefacts. **(b)** With an extra gradient in only the ^{15}N module, i.e. only the ^{13}C artefacts. **(c)** With an extra gradient in only the ^{13}C module. **(d)** With no extra gradients. Spectra were obtained on a 700 MHz Bruker AV III equipped with a TCI H/C/N cryoprobe; the sample used was 40 mM gramicidin in DMSO- d_6 .

Additional information can be gleaned from the following series of CLIP-COSY spectra, obtained from NOAH-2 $S_2^+ C^c$ supersequences. In the seHSQC module, the two gradients g_1 in the t_1 period are independently enabled or disabled (by setting their amplitude to 0). Traces of the resulting CLIP-COSY spectra are shown in Figure S4. The gradients serve to dephase any bulk $^1H^{13}C$ magnetisation that is transverse during either half of t_1 : therefore, if (for example) the gradient in the first half of t_1 is switched off, this allows bulk magnetisation that is transverse in the first half of t_1 to evolve and ultimately contribute to the wing artefacts in the CLIP-COSY. As can be seen, gradients must be applied in *both* halves for complete suppression of the wing artefacts.

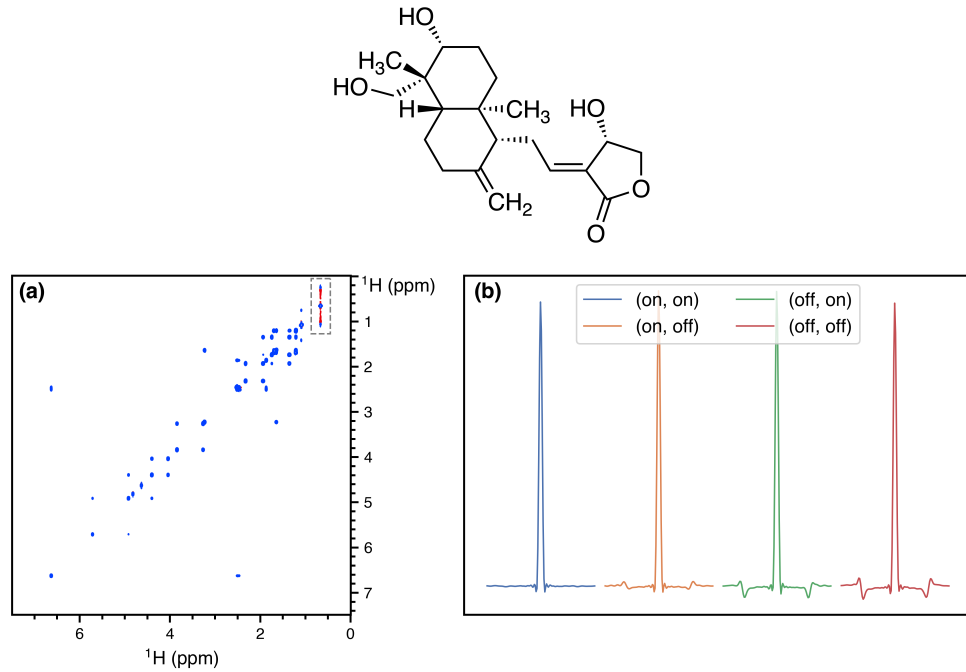


Figure S4: (a) CLIP-COSY spectrum obtained from NOAH-2 $S_2^+ C^c$ sequence, where both gradients in t_1 were disabled (i.e. “(off, off)”). The other three CLIP-COSY spectra are similar, except that the (on, on) spectrum (with gradients applied in both halves of t_1) does not have wing artefacts (grey box). (b) f_1 traces through 0.67 ppm of the four CLIP-COSY spectra obtained with various combinations of gradients, corresponding to the boxed area in (a). Only the (on, on) spectrum (in blue) is free from wing artefacts. The (on, off) and (off, on) spectra (in orange and green respectively) have wing artefacts arising from bulk magnetisation that evolves during the second and first halves of the seHSQC t_1 period respectively. The (off, off) spectrum (red), which corresponds to the 2D spectrum in (a), has the greatest intensity of wing artefacts. Spectra were obtained on a 700 MHz Bruker AV III equipped with a TCI H/C/N cryoprobe; the sample used was 40 mM andrographolide in $DMSO-d_6$.

3 Effect of setting $\Delta' = 1/(4 \cdot {}^1J_{CH})$ in seHSQC

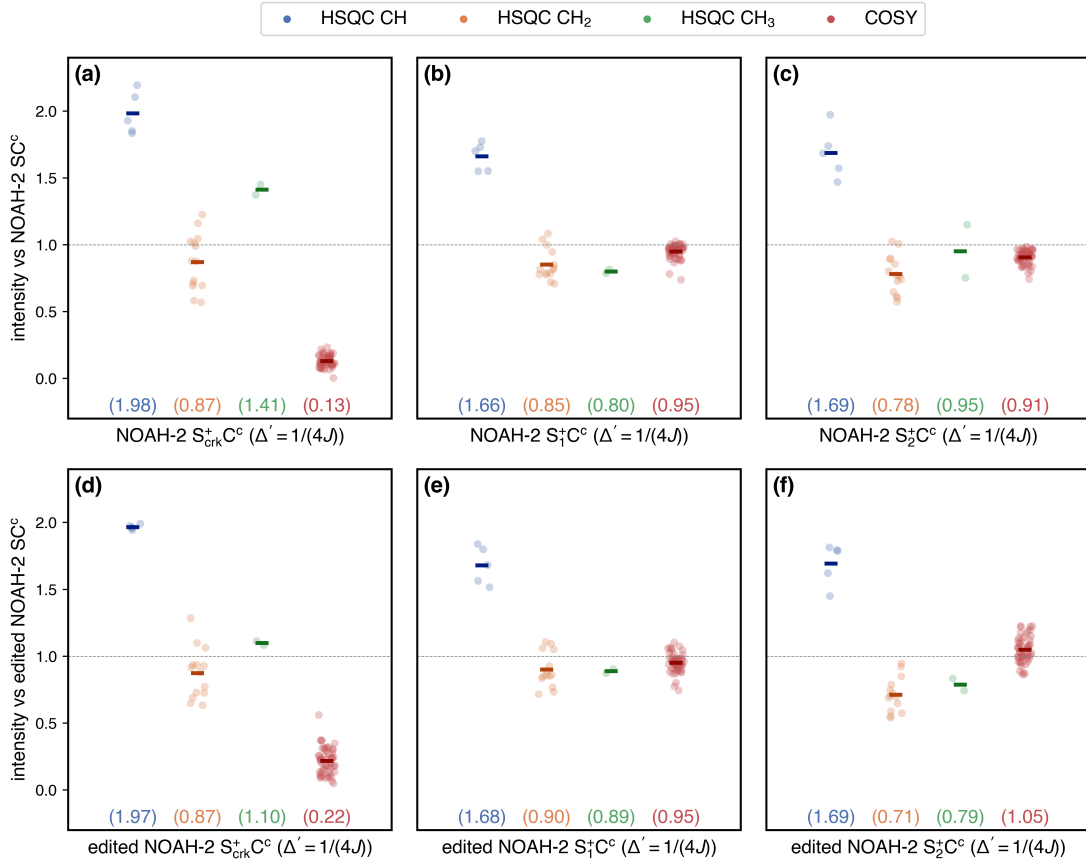


Figure S5: Sensitivity of NOAH-2 S⁺C^c supersequences with Δ' set to $1/(4 \cdot {}^1J_{CH})$, versus the corresponding NOAH-2 SC^c supersequence (i.e. unedited for (a)–(c), edited for (d)–(f)). (a) CRK seHSQC, without multiplicity editing. (b) S₁⁺ module, without multiplicity editing. (c) S₂⁺ module, without multiplicity editing. (d) CRK seHSQC, with multiplicity editing. (e) S₁⁺ module, with multiplicity editing. (f) S₂⁺ module, with multiplicity editing. Spectra were obtained on a 700 MHz Bruker AV III equipped with a TCI H/C/N cryoprobe; the sample used was 40 mM andrographolide in DMSO-*d*₆.

By setting $\Delta' = 1/(4 \cdot {}^1J_{CH})$, theory predicts a larger sensitivity enhancement for CH peaks, whereas CH₂ and CH₃ peaks should have the same sensitivity as in the unenhanced HSQC. This is true for both the S₁⁺ and S₂⁺ modules, as can be seen by comparing Figures 2b and 2c (which show $\Delta' = 1/(8 \cdot {}^1J_{CH})$) to Figures S5b and S5c (which show $\Delta' = 1/(4 \cdot {}^1J_{CH})$). At the same time, for CH₂ and CH₃ peaks, we observe sensitivity *losses* even relative to the unenhanced HSQC; this is likely due to pulse imperfections in the longer pulse sequence and is in line with previous studies (ref. 13 of the main text).

4 Comparison of BIG-BIRD and ZIP elements

The BIG-BIRD element used here was $45^\circ_{45^\circ}(^1\text{H}) - 2\Delta - 180^\circ(^1\text{H}, ^{13}\text{C}) - 2\Delta - 45^\circ_{225^\circ}(^1\text{H})$ for the unedited NOAH seHSQC, where β_ϕ indicates a hard pulse with flip angle β and phase ϕ , and $\Delta = 1/(4 \cdot ^1J_{\text{CH}})$. For the edited NOAH seHSQC, the BIG-BIRD pulse phases are slightly modified to give $45^\circ_{315^\circ}(^1\text{H}) - 2\Delta - 180^\circ(^1\text{H}, ^{13}\text{C}) - 2\Delta - 45^\circ_{135^\circ}(^1\text{H})$. These, and the ZIP, have the same net effect on $^1\text{H}^{\text{C}}$ and $^1\text{H}^{!C}$ magnetisation, as can be seen from the product operator analysis in Figure S1. Thus, they can be used interchangeably in version 2 of the NOAH seHSQC. However, the ZIP provides greater sensitivity in both the HSQC and downstream COSY (Figure S6).

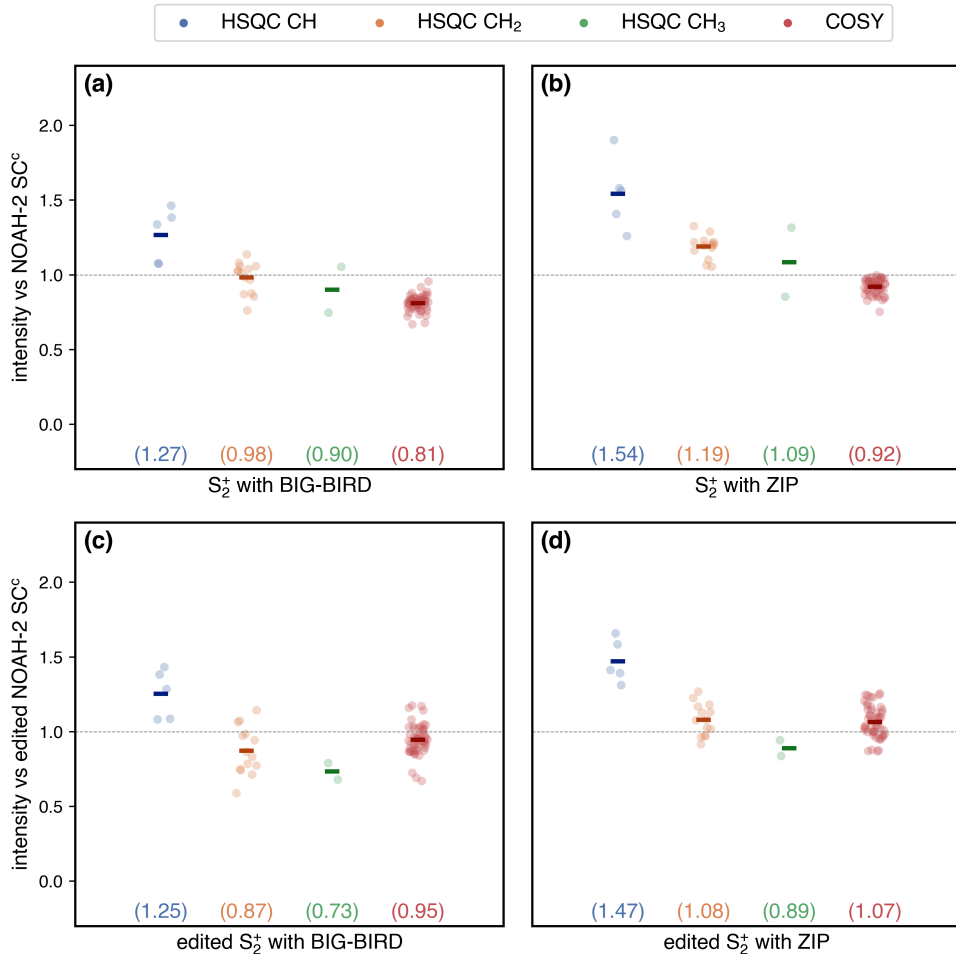


Figure S6: Sensitivity of NOAH-2 $S_2^+ \text{C}^{\text{c}}$ supersequences with either BIG-BIRD or ZIP elements, versus the corresponding NOAH-2 SC^{c} supersequences (i.e. unedited for (a) and (b), edited for (c) and (d)). The value of Δ' was set to $1/(8 \cdot ^1J_{\text{CH}})$. (a) Using the unedited NOAH seHSQC with the BIG-BIRD element. (b) Unedited seHSQC with ZIP. (c) Edited seHSQC with BIG-BIRD. (d) Edited seHSQC with ZIP. Spectra were obtained on a 700 MHz Bruker AV III equipped with a TCI H/C/N cryoprobe; the sample used was 40 mM andrographolide in DMSO-*d*₆.

5 Multiplicity editing in seHSQC

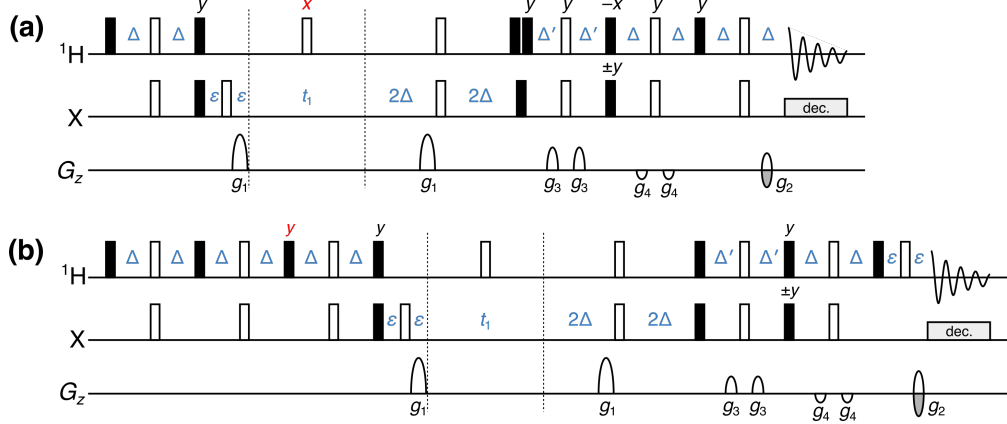


Figure S7: Implementation of multiplicity editing in the new NOAH seHSQC modules. Pulse phases which differ from the unedited versions (Figure S1) are highlighted in red; these are needed to compensate for the extra ^1H 180° pulse in the editing period. Symbols have the same meaning as in Figure 1 of the main text. (a) NOAH seHSQC, version 1 (“ S_1^+ ”). (b) NOAH seHSQC, version 2 (“ S_2^+ ”).

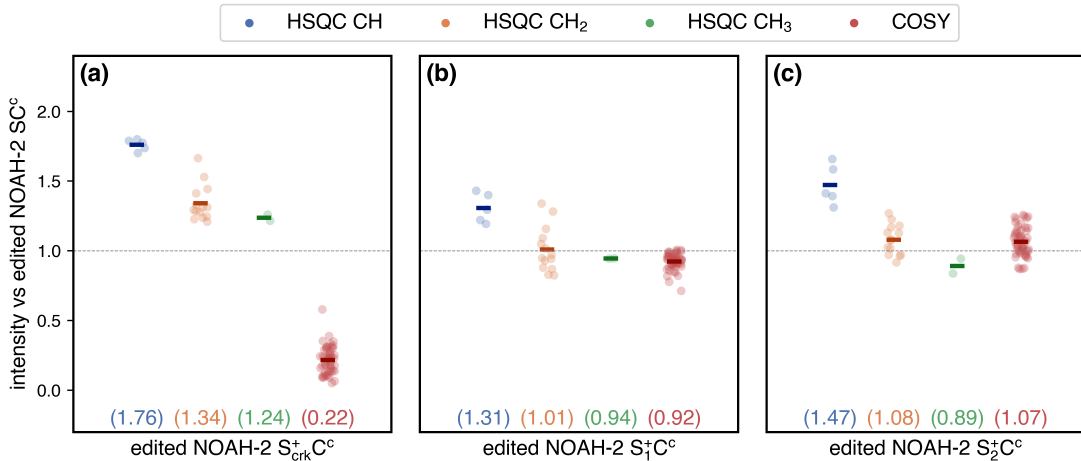


Figure S8: Sensitivity of multiplicity-edited $S^+\text{C}^c$ supersequences, relative to the SC^c supersequence. Spectra were obtained with $\Delta' = 1/(8 \cdot ^1\text{J}_{\text{CH}})$. (a) Using the CRK seHSQC. (b) Using the S_1^+ module. (c) Using the S_2^+ module. Spectra were obtained on a 700 MHz Bruker AV III equipped with a TCI H/C/N cryoprobe; the sample used was 40 mM andrographolide in DMSO- d_6 .

On average, both versions of the NOAH seHSQC provide sensitivity gains for HSQC CH and CH₂ peaks (Figures S8b and S8c) while not compromising the COSY intensities as the CRK seHSQC does (Figure S8a). The S_2^+ module in particular provides slightly better performance. Note also how the COSY intensities with the S_2^+ module are on average higher than with the original HSQC module: this indicates that the S_2^+ module preserves bulk $^1\text{H}^{13}\text{C}$ magnetisation better. As discussed in the main text, this is because the bulk magnetisation is longitudinal during the editing period.

6 Summary of ^{13}C seHSQC sensitivity comparisons

| Experiment | | HSQC | | | COSY | Figure | |
|------------|--------------------|-----------|-------|---------------|---------------|--------|-----|
| edited? | HSQC variant | Δ' | CH | CH_2 | CH_3 | | |
| no | HSQC | – | 1.00* | 1.00* | 1.00* | 1.00* | – |
| | CRK seHSQC | 1/(8J) | 1.80 | 1.32 | 1.58 | 0.13 | 2a |
| | NOAH seHSQC v1 | 1/(8J) | 1.29 | 0.94 | 0.89 | 0.94 | 2b |
| | NOAH seHSQC v2 | 1/(8J) | 1.54 | 1.19 | 1.09 | 0.92 | 2c |
| | CRK seHSQC | 1/(4J) | 1.98 | 0.87 | 1.41 | 0.13 | S5a |
| | NOAH seHSQC v1 | 1/(4J) | 1.66 | 0.85 | 0.80 | 0.95 | S5b |
| | NOAH seHSQC v2 | 1/(4J) | 1.69 | 0.78 | 0.95 | 0.91 | S5c |
| | no HSQC, only COSY | – | – | – | – | 1.09 | – |
| yes | HSQC | – | 1.00† | 1.00† | 1.00† | 1.00† | – |
| | CRK seHSQC | 1/(8J) | 1.76 | 1.34 | 1.24 | 0.22 | S8a |
| | NOAH seHSQC v1 | 1/(8J) | 1.31 | 1.01 | 0.94 | 0.92 | S8b |
| | NOAH seHSQC v2 | 1/(8J) | 1.47 | 1.08 | 0.89 | 1.07 | S8c |
| | CRK seHSQC | 1/(4J) | 1.97 | 0.87 | 1.10 | 0.22 | S5d |
| | NOAH seHSQC v1 | 1/(4J) | 1.68 | 0.90 | 0.89 | 0.95 | S5e |
| | NOAH seHSQC v2 | 1/(4J) | 1.69 | 0.71 | 0.79 | 1.05 | S5f |
| | no HSQC, only COSY | – | – | – | – | 1.29 | – |

Table S1: Relative sensitivities of HSQC and CLIP-COSY spectra in NOAH-2 SC^c and S⁺C^c supersequences. All sensitivities are normalised against the corresponding SC^c sequences: in particular, the unedited seHSQC supersequences are compared against the unedited SC^c (marked with *), and likewise edited seHSQC supersequences are compared against the edited SC^c (marked with †). Note that the two standalone CLIP-COSY entries (the last row in both sections) refer to the same spectrum, and therefore have the same *absolute* sensitivity. The difference in the *relative* sensitivity arises only because they are being compared against the COSY intensities in different reference supersequences, which is done here for consistency with the other figures in this text. See Table S2 for a version of this table where the COSY sensitivities in both unedited and edited supersequences are normalised against the standalone CLIP-COSY. Spectra were obtained on a 700 MHz Bruker AV III equipped with a TCI H/C/N cryoprobe; the sample used was 40 mM andrographolide in DMSO-*d*₆.

| edited? | HSQC variant | Δ' | HSQC | | | COSY |
|---------|--------------------|-----------|-------|-----------------|-----------------|-------|
| | | | CH | CH ₂ | CH ₃ | |
| no | HSQC | – | 1.00* | 1.00* | 1.00* | 0.93 |
| | CRK seHSQC | 1/(8J) | 1.80 | 1.32 | 1.58 | 0.12 |
| | NOAH seHSQC v1 | 1/(8J) | 1.29 | 0.94 | 0.89 | 0.88 |
| | NOAH seHSQC v2 | 1/(8J) | 1.54 | 1.19 | 1.09 | 0.85 |
| | CRK seHSQC | 1/(4J) | 1.98 | 0.87 | 1.41 | 0.12 |
| | NOAH seHSQC v1 | 1/(4J) | 1.66 | 0.85 | 0.80 | 0.88 |
| | NOAH seHSQC v2 | 1/(4J) | 1.69 | 0.78 | 0.95 | 0.84 |
| | no HSQC, only COSY | – | – | – | – | 1.00‡ |
| yes | HSQC | – | 1.00† | 1.00† | 1.00† | 0.79 |
| | CRK seHSQC | 1/(8J) | 1.76 | 1.34 | 1.24 | 0.17 |
| | NOAH seHSQC v1 | 1/(8J) | 1.31 | 1.01 | 0.94 | 0.73 |
| | NOAH seHSQC v2 | 1/(8J) | 1.47 | 1.08 | 0.89 | 0.84 |
| | CRK seHSQC | 1/(4J) | 1.97 | 0.87 | 1.10 | 0.17 |
| | NOAH seHSQC v1 | 1/(4J) | 1.68 | 0.90 | 0.89 | 0.75 |
| | NOAH seHSQC v2 | 1/(4J) | 1.69 | 0.71 | 0.79 | 0.82 |
| | no HSQC, only COSY | – | – | – | – | 1.00‡ |

Table S2: Relative sensitivities of HSQC and CLIP-COSY spectra in NOAH-2 SC^c and S⁺C^c supersequences. All HSQC sensitivities are normalised against the HSQC spectrum in the corresponding SC^c sequences: in particular, the unedited seHSQCs are compared against the unedited HSQC (marked with *), and likewise edited seHSQCs are compared against the edited HSQC (marked with †). All COSY sensitivities are compared against the standalone CLIP-COSY spectrum (the last row in both sections, marked with ‡). This is different from the figures used in this text, which compare the COSY intensities against the COSY component of the corresponding SC^c supersequence. See Table S1 for a version of this table which is consistent with the other figures in this text. Spectra were obtained on a 700 MHz Bruker AV III equipped with a TCI H/C/N cryoprobe; the sample used was 40 mM andrographolide in DMSO-*d*₆.

7 Retention of bulk magnetisation by ^{15}N modules

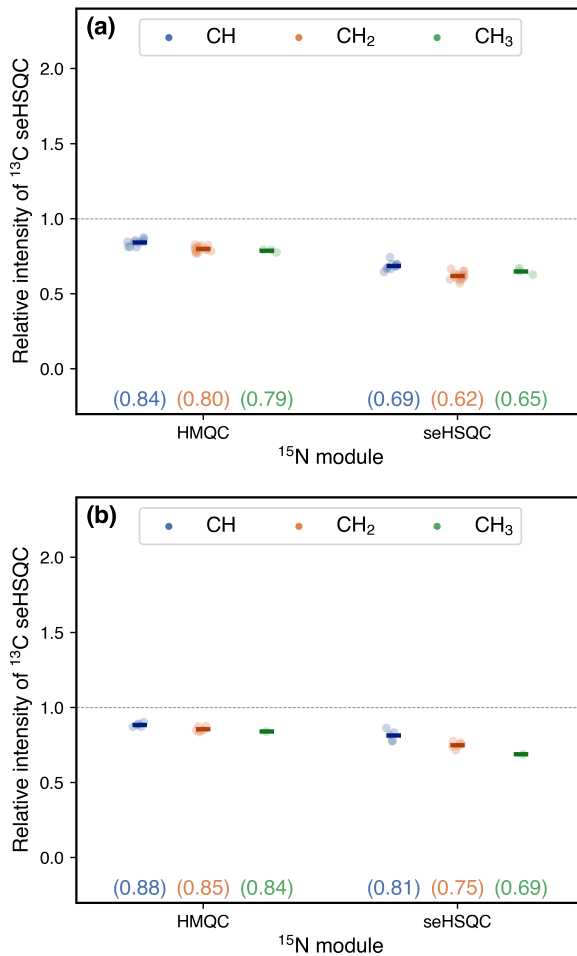


Figure S9: Signal intensities of the ^{13}C seHSQC in NOAH-3 $\text{XS}_2^+ \text{C}^{\text{c}}$ supersequences, normalised against a reference ^{13}C seHSQC taken from a NOAH-2 $\text{S}_2^+ \text{C}^{\text{c}}$ supersequence. The module X is either the ^{15}N HMQC (M) or the ^{15}N seHSQC (S_N^+); the numbers indicate the amount of $^1\text{H}^{\text{C}}$ magnetisation that is preserved by the ^{15}N module. (a) Using 40 mM gramicidin in DMSO- d_6 . (b) Using 50 mM zolmitriptan in DMSO- d_6 . Spectra were obtained on a 700 MHz Bruker AV III equipped with a TCI H/C/N cryoprobe.

8 ^{15}N HSQC and line broadening

For $^{15}\text{N}-^1\text{H}$ correlations, both the HMQC and version 2 of the new seHSQC are recommended as they keep the bulk magnetisation (both $^1\text{H}^{\text{C}}$ and $^1\text{H}^{\text{IX}}$) along $\pm z$ during the t_1 period. The HSQC module, as well as version 1 of the seHSQC, place this magnetisation in the xy -plane during t_1 , leading to J_{HH} evolution; consequently, the amount of bulk magnetisation “passed on” to the downstream modules decreases as the ^{15}N t_1 is increased. Since t_1 for each NOAH module is incremented in sync, this is manifested in downstream modules as a t_1 -dependent decrease in amplitude, or f_1 line broadening after Fourier transformation, as shown in Figure S10.

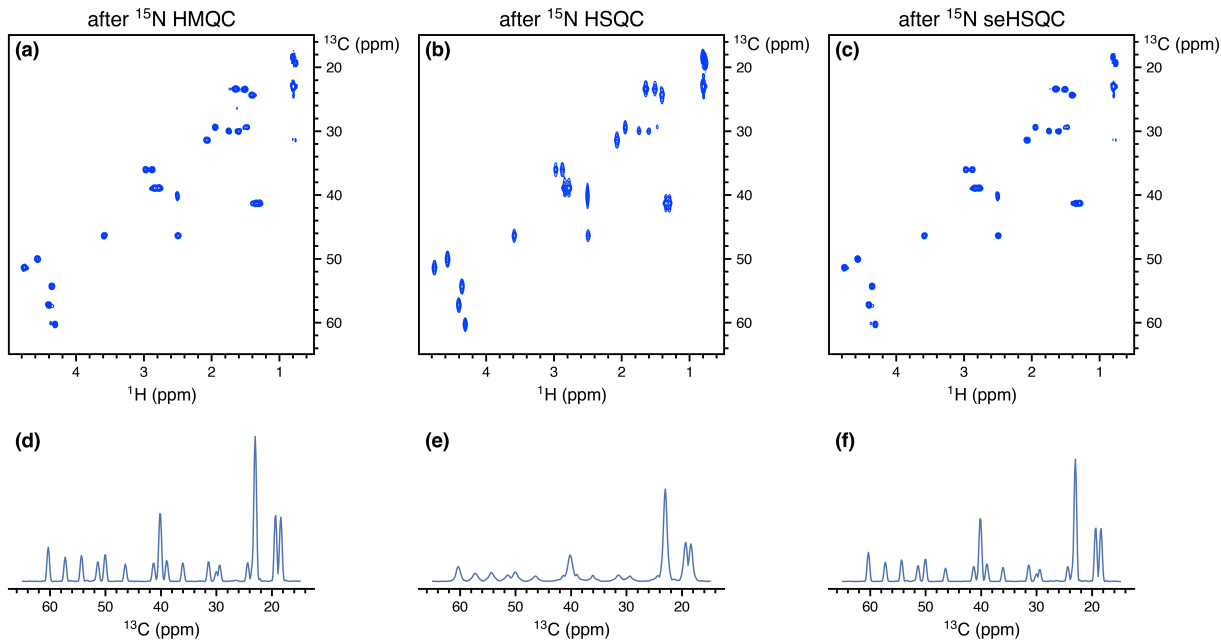


Figure S10: ^{13}C seHSQC spectra obtained from NOAH-3 XS₂⁺C^c (^{15}N module + ^{13}C seHSQC + CLIP-COSY) supersequences. The ^{15}N spectral window was 30 ppm and 256 t_1 increments were collected, corresponding to an indirect-dimension ^{15}N acquisition time of 60.1 ms. (a) X = HMQC (“M”). (b) X = HSQC (“S”). (c) X = seHSQC (“S_N⁺”). (d)–(f) Projections of spectra (a)–(c) onto the f_1 axis. Note the f_1 line broadening in (b) and (e). Spectra were obtained on a 700 MHz Bruker AV III equipped with a TCI H/C/N cryoprobe; the sample used was 40 mM gramicidin in DMSO-*d*₆.

This line broadening also leads to a substantial sensitivity loss (for example, across all peaks, the ^{13}C seHSQC in Figure S10b has almost 65% lower sensitivity than that in Figure S10a). The extent of the line broadening depends on the acquisition time, and is particularly pronounced for long acquisition times, i.e. small ^{15}N spectral windows. In our experience, at ^{15}N acquisition times of ca. 5 ms the effect is almost indiscernible. Such a short acquisition time would lead to poor resolution in the ^{15}N dimension itself, which may or may not be tolerable. Of course, this issue can be entirely avoided by using either the HMQC or seHSQC.

9 Effect of lengthened gradients in ^{15}N modules

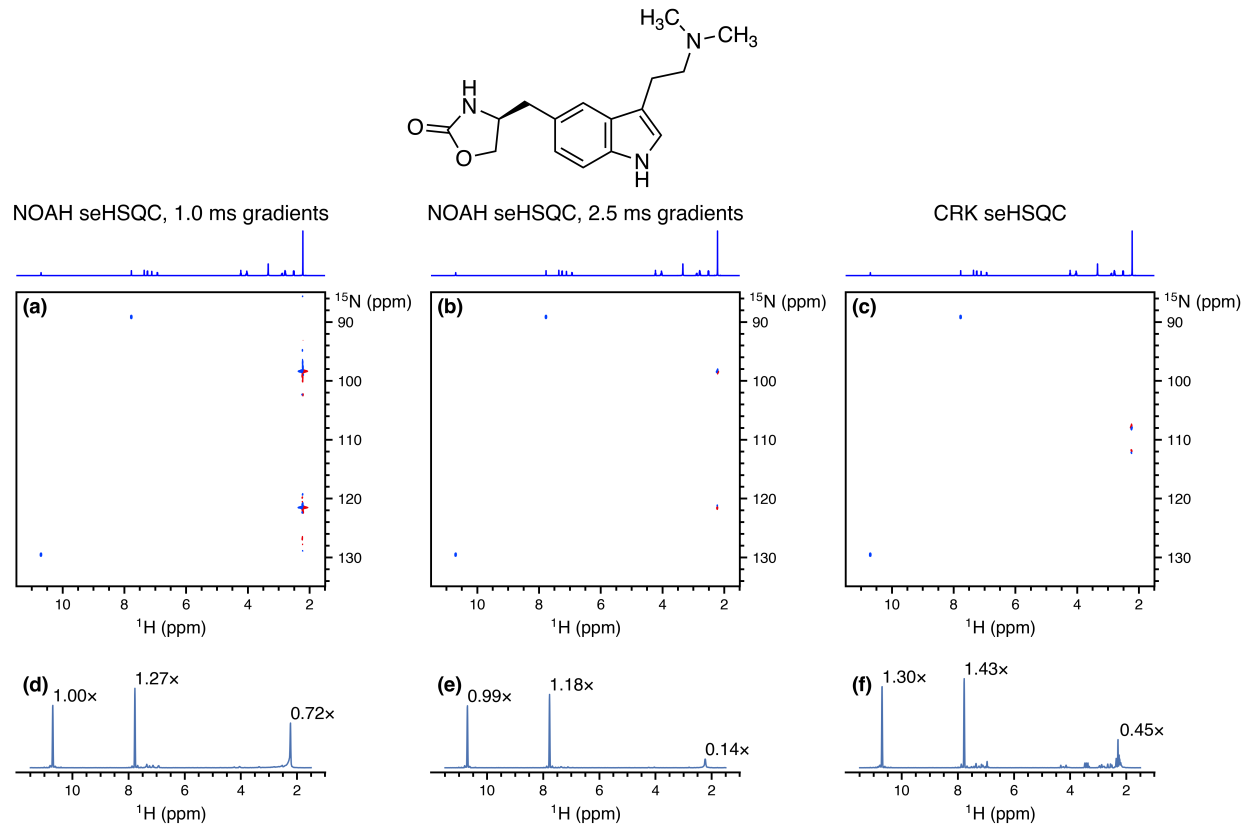


Figure S11: ^{15}N seHSQC spectra obtained using the NOAH and CRK implementations. The peaks at 7.8 and 10.7 ppm (^1H shifts) are genuine crosspeaks; the mixed-phase peaks at 2.2 ppm are artefacts. The 1D ^1H spectrum is shown above each of the 2D spectra in (a)–(c); the artefacts seen in the 2D correspond to the intense N -methyl groups at 2.2 ppm. (a) NOAH seHSQC, with original CTP gradients of 1 ms. (b) NOAH seHSQC, with longer CTP gradients of 1 ms. (c) Standalone CRK seHSQC with 1 ms CTP gradients (Bruker `hsqcetf3gpsi2` pulse programme). (d)–(f) Projections of spectra (a)–(c) onto the f_2 axis. The numbers indicate relative peak heights (normalised against the 10.7 ppm peak in (d)). Spectra were obtained on a 700 MHz Bruker AV III equipped with a TCI H/C/N cryoprobe; the sample used was 50 mM zolmitriptan in $\text{DMSO}-d_6$.

The lengthening of CTP gradients from 1 ms to 2.5 ms is aimed at cleaning up artefacts arising from bulk magnetisation that is not properly returned to $+z$ at the end of the sequence. Figure S11 shows exactly how effective this strategy is. In (d), where the CTP gradients have their original duration, the artefacts originating from the intense methyl groups have comparable intensity to the desired peaks. When the gradients are lengthened in (e), the crosspeak intensities are almost unaffected, whereas the artefacts are suppressed by a factor of 5 or more. Although this suppression is not complete, this should not be interpreted as a weakness of the new NOAH seHSQC module, as similar artefacts are also visible in the CRK seHSQC (f). Indeed, every ^{15}N – ^1H experiment we tested has at least *some* artefact intensity in this region.

10 Effect of k -scaling

The effect of k -scaling on the HMQC is shown in Figure S12. By decreasing the indirect dimension resolution, the f_1 linewidths of the peaks increase: this can lead to significant sensitivity enhancement for the HMQC (up to $2.7\times$), because J_{HH} splitting in the f_1 dimension is no longer resolved. The largest gains are observed for peaks where J_{HH} splitting is more visible; for the leftmost peak at $\delta_N = 128$ ppm which has no resolved J_{HH} splitting, only a more modest $1.7\times$ gain in sensitivity is attained.

For the seHSQC module, k -scaling on its own leads to far smaller sensitivity gains (Figure S13). Any increase in the total peak volume is almost completely offset by the f_1 broadening. Therefore, even at $k = 8$, the largest sensitivity gains that can be attained are $\sim 1.3\times$.

The use of linear prediction for spectra with $k > 1$ can, to a certain extent, compensate for the line broadening. This is less successful for the HMQC spectra (Figure S14). Although raw gains in peak height can be observed for all values of k , there is a corresponding decrease in the spectral quality, as evidenced by the f_1 multiplet structure being increasingly distorted. On the other hand, linear prediction performs well for the seHSQC spectra (Figure S15), where there is no multiplet structure in f_1 . Even the reconstruction with $k = 8$ has reasonable spectral quality: although the 2D spectrum (d) appears to have unusual peak shapes, this is merely the result of having the same contour levels as the $k = 1$ spectrum. The actual peaks are still clearly singlets, as can be seen from the projection in (h).

An additional example of successful k -scaling and linear prediction (with $k = 4$) can be seen in Section 12.

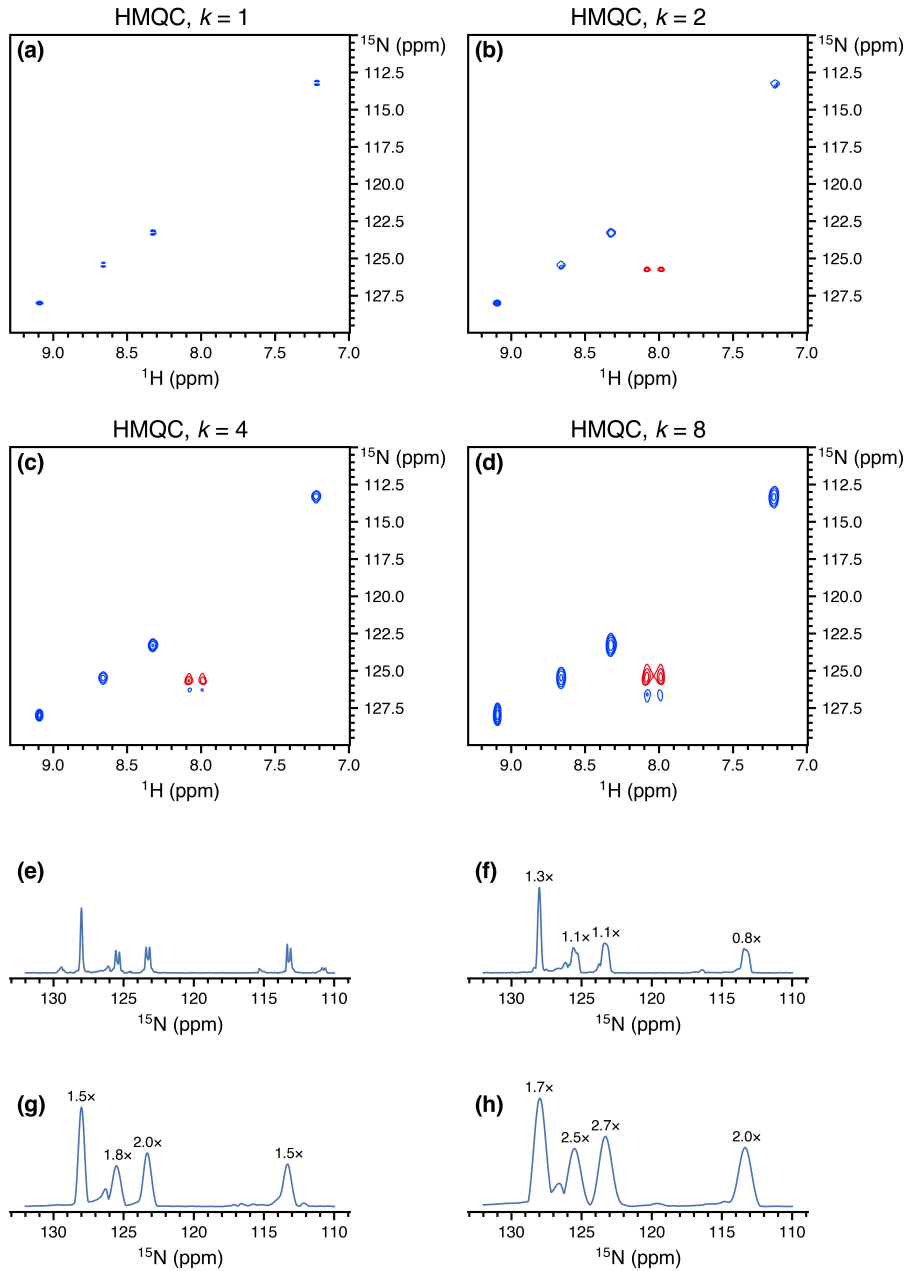


Figure S12: (HMQC without linear prediction.) ¹⁵N HMQC spectra (from NOAH-3 MS₂⁺C^c supersequences) obtained with various values of the scaling factor k . The peak at $\delta_{\text{H}} = 8.03$ ppm is a folded peak from the ornithine $\delta\text{-NH}_2$. (a) $k = 1$, with 256 t_1 increments and 2 scans per increment (denoted as 256 : 2). (b) $k = 2$, i.e. effectively 128 t_1 increments and 4 scans per increment (128 : 4). (c) $k = 4$ (64 : 8). (d) $k = 8$ (32 : 16). (e)–(h) Projections of 2D spectra in (a)–(d) onto the f_1 axis, shown at the same noise level. Numbers indicate peak heights relative to the $k = 1$ HMQC spectrum. Spectra were obtained on a 700 MHz Bruker AV III equipped with a TCI H/C/N cryoprobe; the sample used was 40 mM gramicidin in DMSO-*d*₆.

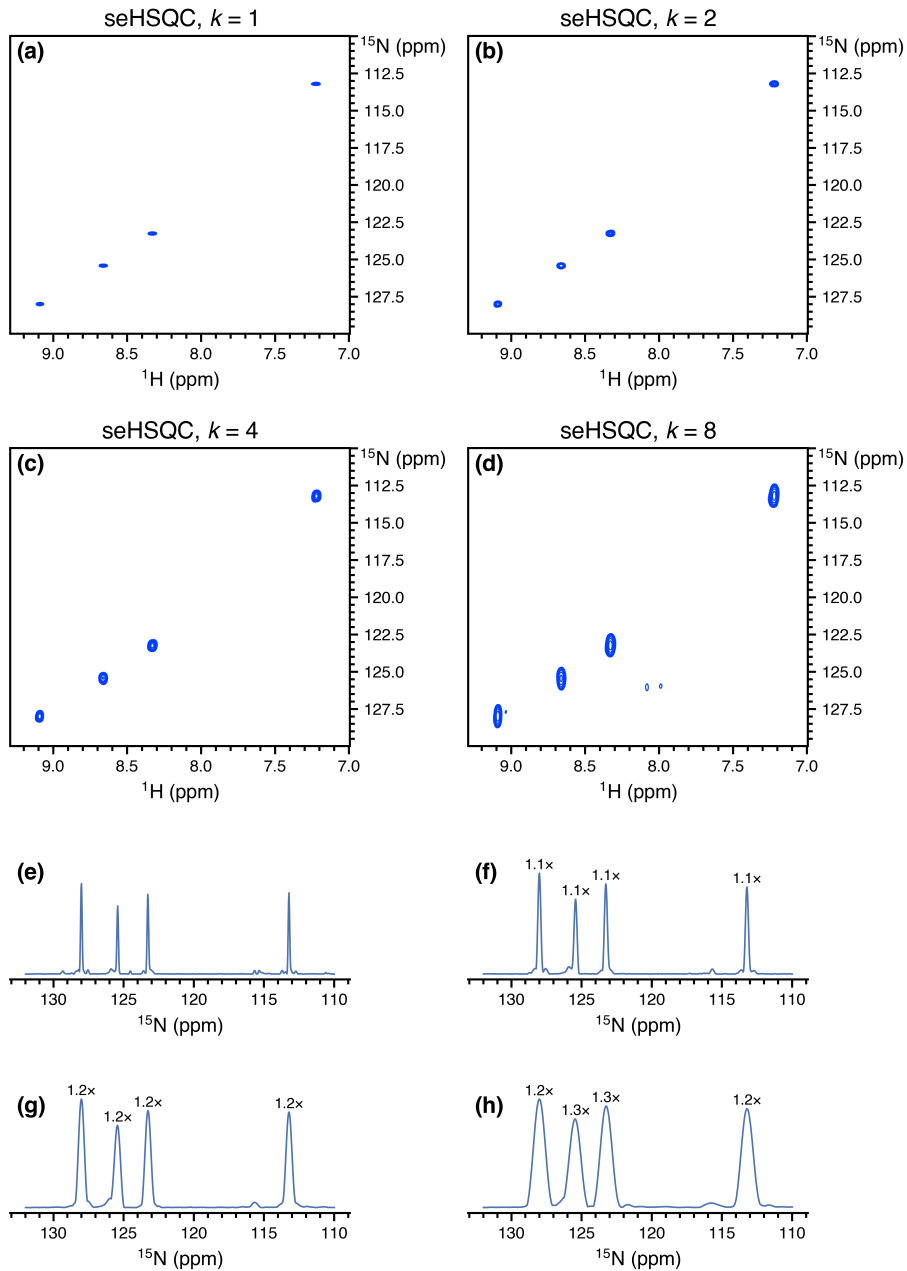


Figure S13: (seHSQC without linear prediction.) ¹⁵N seHSQC spectra (from NOAH-3 S_N⁺S₂⁺C^c super-sequences) obtained with various values of the scaling factor *k*. The peak at $\delta_{\text{H}} = 8.03$ ppm is a folded peak from the ornithine δ -NH₂. (a) *k* = 1 (256 *t*₁ increments, 2 scans each). (b) *k* = 2 (128 : 4). (c) *k* = 4 (64 : 8). (d) *k* = 8 (32 : 16). (e)–(h) Projections of 2D spectra in (a)–(d) onto the *f*₁ axis, shown at the same noise level. Numbers indicate peak heights relative to the *k* = 1 seHSQC spectrum. Spectra were obtained on a 700 MHz Bruker AV III equipped with a TCI H/C/N cryoprobe; the sample used was 40 mM gramicidin in DMSO-*d*₆.

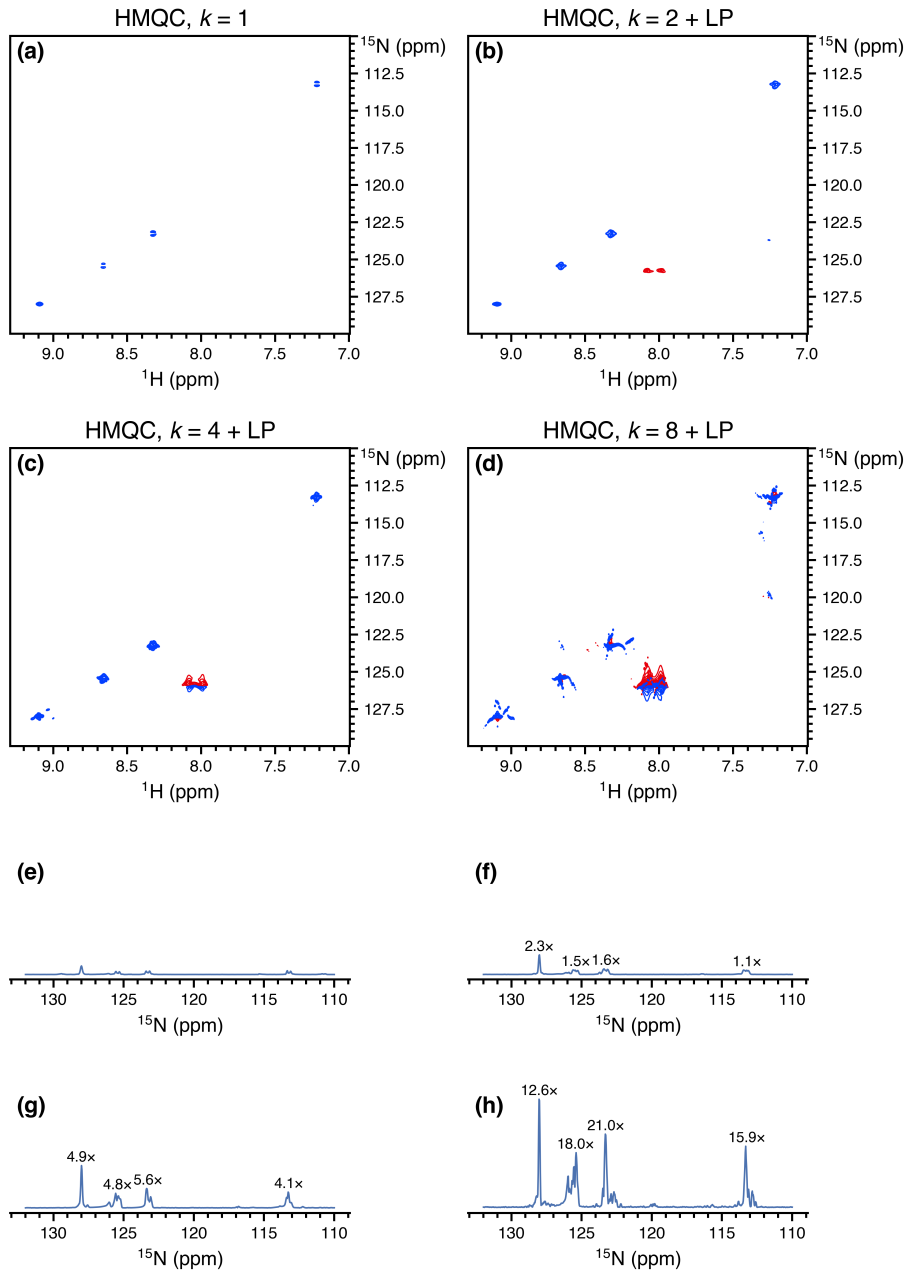


Figure S14: (HMQC with linear prediction.) ^{15}N HMQC spectra (from NOAH-3 $\text{MS}_2^+\text{C}^\text{c}$ supersequences) obtained with various values of the scaling factor k , after linear prediction up to 512 complex points in f_1 . The peak at $\delta_{\text{H}} = 8.03$ ppm is a folded peak from the ornithine $\delta\text{-NH}_2$. (a) $k = 1$ (256 : 2). Note that this spectrum is the same as in Figure S12a. (b) $k = 2$ (128 : 4). (c) $k = 4$ (64 : 8). (d) $k = 8$ (32 : 16). (e)–(h) Projections of 2D spectra in (a)–(d) onto the f_1 axis, shown at the same noise level. Numbers indicate peak heights relative to the $k = 1$ HMQC spectrum. Spectra were obtained on a 700 MHz Bruker AV III equipped with a TCI H/C/N cryoprobe; the sample used was 40 mM gramicidin in $\text{DMSO}-d_6$.

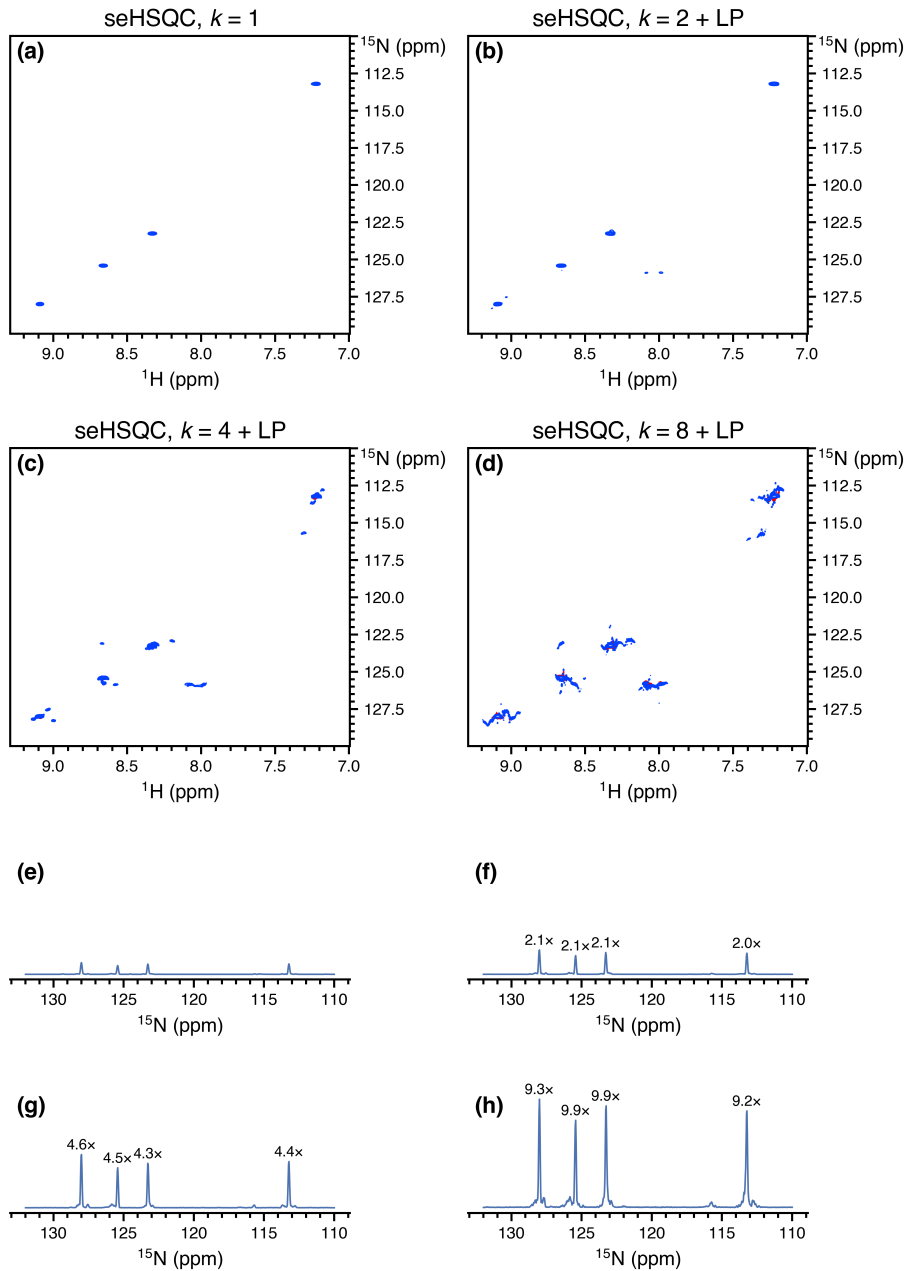


Figure S15: (seHSQC with linear prediction.) ¹⁵N seHSQC spectra (from NOAH-3 S_N⁺S₂⁺C^c supersequences) obtained with various values of the scaling factor k , after linear prediction up to 512 complex points in f_1 . The peak at $\delta_H = 8.03$ ppm is a folded peak from the ornithine $\delta\text{-NH}_2$. (a) $k = 1$ (256 : 2). Note that this spectrum is the same as in Figure S13a. (b) $k = 2$ (128 : 4). (c) $k = 4$ (64 : 8). (d) $k = 8$ (32 : 16). (e)–(h) Projections of 2D spectra in (a)–(d) onto the f_1 axis, shown at the same noise level. Numbers indicate peak heights relative to the $k = 1$ seHSQC spectrum. Spectra were obtained on a 700 MHz Bruker AV III equipped with a TCI H/C/N cryoprobe; the sample used was 40 mM gramicidin in DMSO-*d*₆.

11 HSQC-TOCSY/HSQC sensitivity comparisons

The signal intensities for the NOAH-3 S^TSC^c (HSQC-TOCSY + HSQC + CLIP-COSY) supersequences can be more conveniently measured by omitting the DIPSI-2 isotropic mixing in the HSQC-TOCSY supersequence, leading to a NOAH-3 SSC^c (HSQC + HSQC + CLIP-COSY) supersequence. This allows us to compare the different versions of double-HSQC sequences, as the two HSQC modules can be implemented either using the MFA approach, or the new ASAP/NOAH approach based on Ernst angle excitation in the first module. In the latter implementation, the parameter f can be varied between 0.4 and 1; it represents the proportion of $^1\text{H}^{\text{C}}$ magnetisation used in the first HSQC, as described in the main text. Furthermore, to boost the sensitivity of the second HSQC module in the NOAH supersequences, either of the two new seHSQC modules can be used in its place: we demonstrate this here with the ZIP-seHSQC (S_2^+).

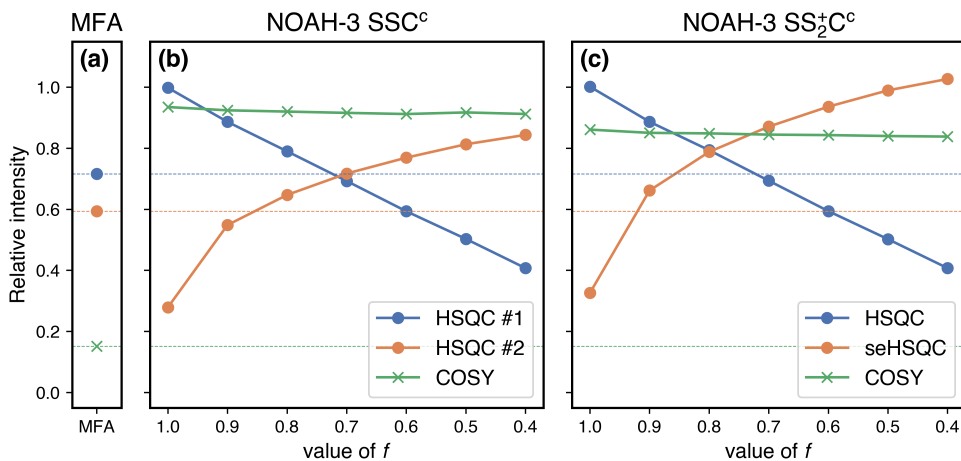


Figure S16: Sensitivities of HSQC and CLIP-COSY modules when used as part of a SSC^c-type supersequence, with both the NOAH and MFA implementations of the two HSQC modules. Intensities are calculated relative to the HSQC and CLIP-COSY modules in a standard NOAH-2 SCc supersequence (averaged over all peaks). (a) Sensitivity of the MFA implementation (i.e. a MFA double HSQC experiment immediately followed by a CLIP-COSY). Horizontal dashed lines at these levels are drawn across all subplots to guide the eye. (b) Sensitivity of NOAH-3 SSC^c modules as a function of f . Note that at $f = 0.8$, all of the NOAH spectra have a greater average sensitivity than their MFA counterparts. (c) Sensitivity of NOAH-3 SS₂⁺CC^c modules as a function of f . Spectra were obtained on a 700 MHz Bruker AV III equipped with a TCI H/C/N cryoprobe; the sample used was 40 mM andrographolide in DMSO-*d*₆.

Figure S16 may be understood in the following way:

- The MFA HSQC sensitivities (in (a)) are approximately half that of a standard CRK seHSQC, with the second HSQC having slightly lower sensitivity. This is discussed in ref. 17 of the main text.
- The sensitivity of the first NOAH HSQC (blue in (b) and (c)) is generally equal to f , sup-

porting the interpretation of f as the fraction of $^{13}\text{C}-^1\text{H}$ magnetisation excited in the first HSQC.

- The sensitivity of the second NOAH HSQC (orange in (b)) arises from whatever is *not* used by the first HSQC, plus any magnetisation that relaxes during the FID of the first HSQC. As f is decreased, the former contribution increases and the latter tapers off. This is true for the seHSQC as well (orange in (c)), except that there is a uniform boost in sensitivity for all values of f . This sensitivity improvement mainly applies to CH groups, as discussed in the main text.
- The MFA COSY sensitivity (green) is substantially lower ($\sim 15\%$) because the bulk magnetisation is dephased by the previous modules, whereas in the NOAH approach it is (largely) preserved.

It remains to evaluate the impact of adding DIPSI-2 mixing in one of the HSQC modules on the remaining modules in the supersequence. This depends on whether the HSQC-TOCSY module is placed first ($\text{S}^\text{T}\text{SC}^\text{c}$ or $\text{S}^\text{T}\text{S}_2^\text{+}\text{C}^\text{c}$) or second ($\text{SS}_2^\text{T}\text{C}^\text{c}$) in the sequence. Since neither of the new seHSQC modules do preserve unused $^1\text{H}^\text{C}$ magnetisation, the HSQC-TOCSY in a hypothetical $\text{S}^\text{+}\text{S}^\text{T}\text{C}^\text{c}$ supersequence will have greatly reduced sensitivity. On the other hand, placing the HSQC-TOCSY sequence first allows the seHSQC module to be used subsequent to this; we therefore consider only the permutations where the HSQC-TOCSY goes first.

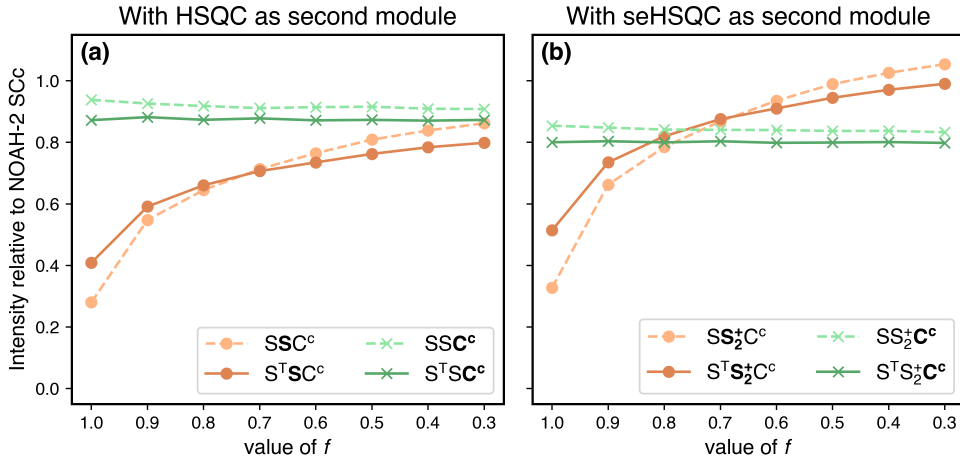


Figure S17: Comparison of signal intensities of second (HSQC or seHSQC) and third (CLIP-COSY) modules in the $\text{S}^\text{T}\text{SC}^\text{c}$ and $\text{S}^\text{T}\text{S}_2^\text{+}\text{C}^\text{c}$ supersequences, versus their intensities in the SSC^c and $\text{SS}_2^\text{+}\text{C}^\text{c}$ sequences, as a function of the parameter f . The solid, darker lines indicate the supersequences beginning with the HSQC-TOCSY, whereas the dashed, lighter lines indicate the supersequences beginning with the HSQC (the latter are the same graphs as in Figure S16). **(a)** With the HSQC as the second module. **(b)** With the seHSQC as the second module. Spectra were obtained on a 700 MHz Bruker AV III equipped with a TCI H/C/N cryoprobe; the sample used was 40 mM andrographolide in $\text{DMSO}-d_6$.

It can be seen from Figure S17 that the introduction of DIPSI-2 mixing leads to a very small drop (< 10%) in the amount of $^1\text{H}^{1\text{C}}$ magnetisation preserved for the COSY module. On the other hand, the HSQC (and seHSQC) sensitivities follow largely the same trend as before. For values of f above 0.7 (where relatively little $^1\text{H}^{1\text{C}}$ magnetisation is preserved for these modules), the DIPSI-2 mixing helps to replenish some of this magnetisation. As f decreases, this effect becomes smaller, and at small f it even leads to a reduction in signal intensity. As discussed in the main text, since the HSQC-TOCSY has a lower intrinsic sensitivity than the (se)HSQC, we recommend using a large value of f , such as 0.9. This does not compromise the HSQC-TOCSY intensity by much, and at the same time yields either a HSQC with $\sim 60\%$ of its original sensitivity, or a seHSQC which has $\sim 75\%$ of the sensitivity of a standard NOAH HSQC.

If the sensitivity of the HSQC-TOCSY component is to be maximised, then it is advisable to use the seHSQC-TOCSY module, which is based on the S_2^+ module and is described in ref. 14 of the main text. This module cannot preserve any $^1\text{H}^{1\text{C}}$ magnetisation for the downstream HSQC, but does retain $^1\text{H}^{1\text{C}}$ magnetisation for homonuclear modules: its performance in this respect is therefore very similar to the HSQC-TOCSY with $f = 1$ (Figure S18). However, it provides greater sensitivity in the HSQC-TOCSY component itself, so is strictly better than the HSQC-TOCSY with $f = 1$.

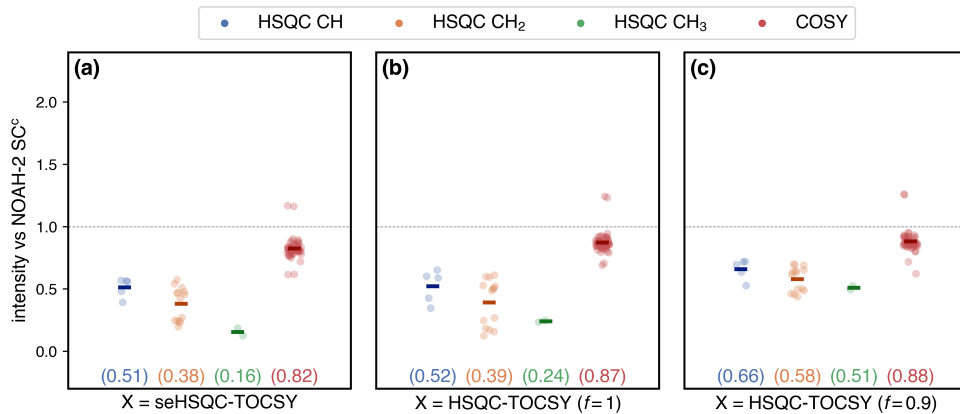


Figure S18: HSQC and COSY intensities in NOAH-3 XSC^c supersequences, where X is a HSQC-TOCSY variant, normalised against the intensities of the NOAH-2 SC^c. (a) With X as the seHSQC-TOCSY module, derived from the S_2^+ sequence. (b) With the unenhanced HSQC-TOCSY module ($f = 1$). Note that this provides no improvement over the seHSQC-TOCSY in the downstream HSQC and COSY modules. (c) With the unenhanced HSQC-TOCSY module ($f = 0.9$). This retains a portion of unused $^1\text{H}^{1\text{C}}$ magnetisation for the second HSQC, resulting in higher intensities. Spectra were obtained on a 700 MHz Bruker AV III equipped with a TCI H/C/N cryoprobe; the sample used was 40 mM andrographolide in DMSO-*d*₆.

Finally, we note that because a significant proportion of the HSQC signal derives from $^1\text{H}^{1\text{C}}$ relaxation during the HSQC-TOCSY FID, use of a longer acquisition time (AQ) can potentially boost the HSQC sensitivity even further. The experiments shown above were carried out with a relatively short AQ of 73 ms. **However, bear in mind that the high duty cycle associated**

with broadband ^{13}C decoupling can potentially damage the probe if applied for too long, especially given that the supersequences described here have two consecutive ^{13}C -decoupled modules.

12 Other example spectra

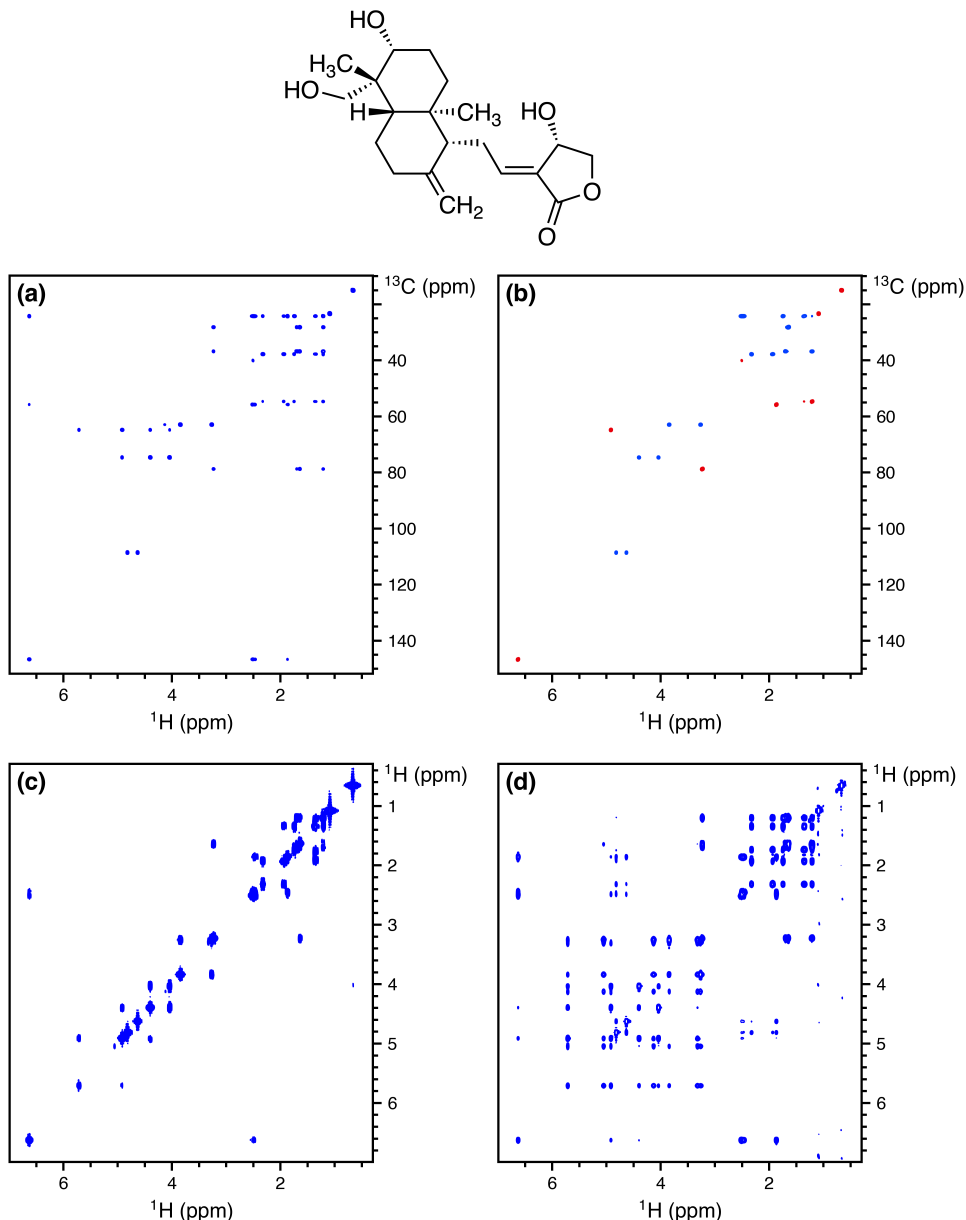


Figure S19: 2D spectra acquired using the NOAH-4 $S^T S_2^+ CT$ supersequence. 256 t_1 increments were used with 2 scans per increment, leading to a total experiment time of 17 minutes and 32 seconds. This represents a 3.25 \times time saving relative to conventional acquisition of each of the four spectra with the same parameters, which would take a total of 57 minutes and 3 seconds. (a) HSQC-TOCSY (30 ms mixing time, $f = 0.9$). (b) Multiplicity edited seHSQC. (c) COSY. (d) TOCSY (60 ms mixing time). Spectra were obtained on a 700 MHz Bruker AV III equipped with a TCI H/C/N cryoprobe; the sample used was 40 mM andrographolide in DMSO- d_6 .

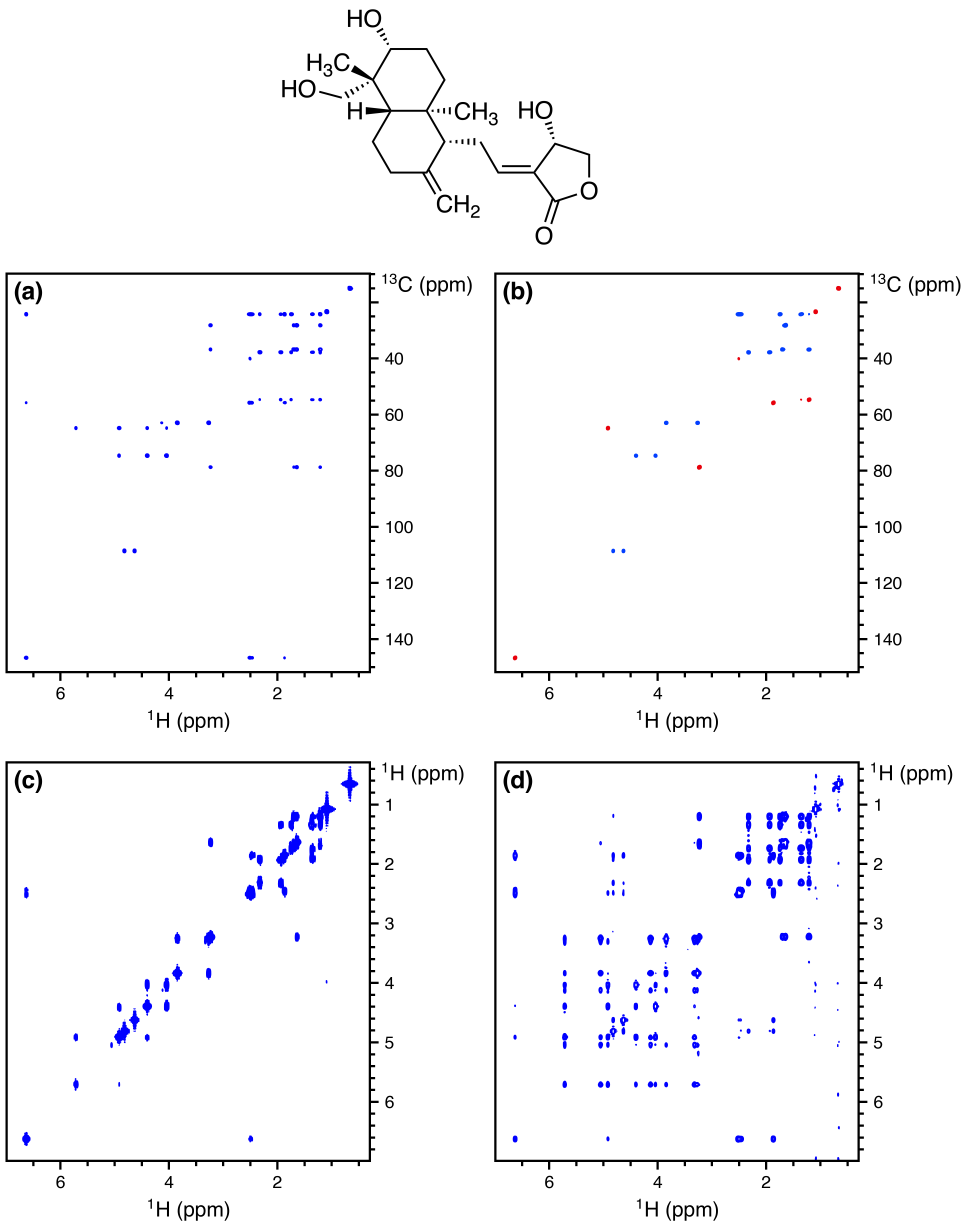


Figure S20: 2D spectra acquired using the NOAH-4 S^TS₂⁺CT supersequence with 50% non-uniform sampling for all modules. All other parameters are the same as in Figure S19. The experimental time was 9 minutes and 1 second. **(a)** HSQC-TOCSY (30 ms mixing time, $f = 0.9$). **(b)** Multiplicity edited seHSQC. **(c)** COSY. **(d)** TOCSY (60 ms mixing time). Spectra were obtained on a 700 MHz Bruker AV III equipped with a TCI H/C/N cryoprobe; the sample used was 40 mM andrographolide in DMSO-*d*₆.

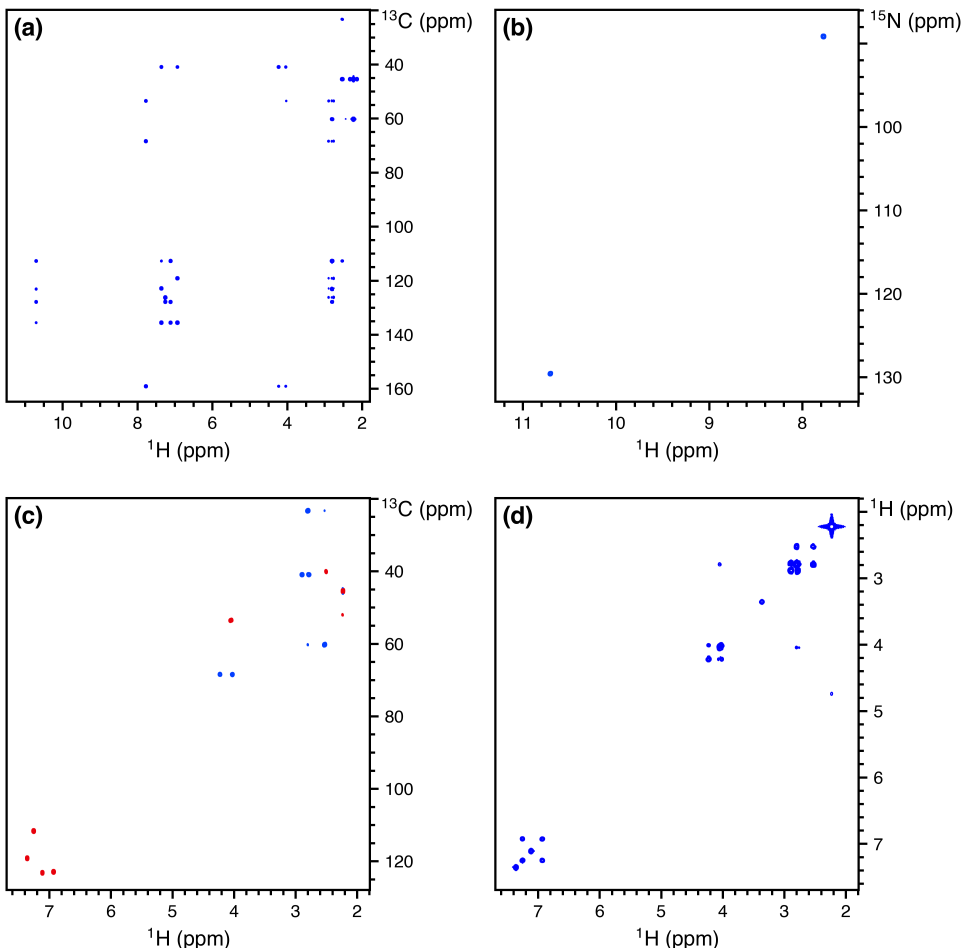
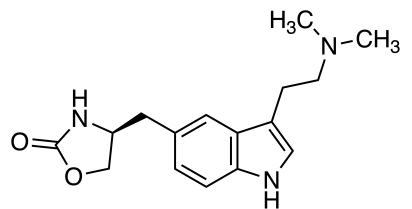


Figure S21: 2D spectra acquired using the NOAH-4 BS_{N2}S₂⁺C supersequence. 256 t_1 increments were used with 2 scans per increment, leading to a total experiment time of 17 minutes and 32 seconds. This represents a 3.22× time saving relative to conventional acquisition of each of the four spectra with the same parameters, which would take a total of 56 minutes and 28 seconds. (a) HMBC. (b) ¹⁵N seHSQC with $k = 4$, linear projected to 512 complex points. (c) Multiplicity edited ¹³C seHSQC. (d) Magnitude-mode COSY (Bruker qf mode). Spectra were obtained on a 700 MHz Bruker AV III equipped with a TCI H/C/N cryoprobe; the sample used was 50 mM zolmitriptan in DMSO-*d*₆.